CONTROL SYSTEM DESIGNS FOR THE SHUTTLE INFRARED TELESCOPE FACILITY

by

J. David Powell
Eric K. Parsons
Kenneth R. Lorell

Guidance and Control Laboratory
Department of Aeronautics and Astronautics
Stanford University

Prepared for

NASA Ames Research Center
Moffett Field, California 94305

Grant NSG-2246

October 1979

I. INTRODUCTION

The Shuttle Infrared Telescope Facility (SIRTF) is being designed as a 1.2 meter, cryogenically cooled, infrared telescope to be flown as a Shuttle-attached payload in the mid-1980's [1]. The SIRTF, mounted in the Orbiter bay on the European Instrument Pointing System (IPS) will make possible previously unobtainable photometric and spectrographic observations over a wide range of IR wavelengths [2].

In order to maximize the effectiveness of SIRTF as a scientific instrument, the optical axis is required to be pointed with an absolute accuracy of 1 arcsecond while the image at the focal plane must remain stable to 0.1 arcseconds [3]. The signal-to-noise ratio during the observation of faint sources is further enhanced by chopping the incoming beam with an oscillating mirror located in the optical train. The modulated image has the same accuracy and stability requirements as the unchopped one. These stringent pointing and stability requirements are further complicated by the demands that infrared astronomy and the SIRTF in particular place on the design of the pointing system.

Primary among the factors which add complexity to the analysis and design of the SIRTF controller are the telescope's cryogenically cooled optics required to avoid thermal interference with the extremely sensitive IR detectors at the focal plane. The entire internal structure of the telescope operates at a temperature of 8°K and below. This low temperature is made possible by a concentric shell design in which the inner optical portion of the telescope is connected to the outer structural cylinder by thin, thermally resistive members, thus minimizing heat transfer losses [4]. Unfortunately, the mechanical coupling between the SIRTF mounting fixture and the optical system is relatively light and flexible, making precise knowledge of the optical axis uncertain.

A second difficulty peculiar to infrared astronomy, and the source of a major shortcoming of previous IR telescope pointing systems, is the lack of a visible component associated with many infrared objects. These objects are therefore not visible to the astronomer, nor can the pointing system use them for augmentation of the basic gyrostabilization loops as is often done in optical astronomy. Tracking a nearby visible object is of course possible, but multiple star trackers are

then required to provide three-axis error information. Even when multiple star trackers are used to provide the off-axis tracking function, the problems of target identification and limited interaction with the control system still remain.

The SIRTF will be mounted on the IPS in the Orbiter bay. The most recent simulations of IPS operation have indicated that while quiescent performance is in the 1-2 arcsecond range, disturbance errors may be as large as 3 arcseconds [5]. Thus, although the IPS can provide positioning for target acquisition and a stable base to isolate the SIRTF from large amplitude Shuttle disturbances, it does not provide the necessary precision or stability for the SIRTF. Additionally, the image dissector tube star trackers utilized by the IPS have no star field display capability.

A number of areas are therefore apparent which pose a design challenge to the efficient operational use of an infrared telescope mounted on the IPS. They are:

the thermal distortion due to temperature differentials between the inner and outer telescope sections;

the light mechanical coupling between the inner and outer telescope shells;

the difficulty of providing off-axis pointing using current star tracker systems;

the lack of a star field display for the operator;

the inability of the IPS to meet the SIRTF fundamental pointing and stability requirements.

The present work deals with the development of an image motion compensation (IMC) system, internal to the SIRTF, which provides the stability and control to meet the SIRTF's pointing requirements. This system uses a charge coupled device (CCD) array located at the SIRTF focal plane combined with outputs from the IPS gyros to drive a mirror in the telescope optical train. The operation of the CCD and the IMC system is controlled by a small, high performance microcomputer whose extremely fast cycle time permits tracking multiple stars and the calculation of error commands for all three axes.

The SIRTF IMC is based in part upon the Video Inertial Pointing (VIP) system developed from 1974 to 1977 at the NASA Ames Research Center [6,7]. The VIP system also utilized a CCD to track multiple stars and combined the star tracker information with gyro outputs. However, the concept of steering a mirror inside the telescope is a major difference between VIP and the SIRTF/IMC. In part, the steering mirror concept evolved due to the stringent SIRTF pointing requirements and because a movable mirror was already part of the SIRTF optical design.

II. SYSTEM DESCRIPTION

The SIRTF/IMC system operates by combining the outputs of the IPS gyros with measurements from a CCD array at the telescope focal plane. The gyros provide a high bandwidth, low noise signal yielding good short term stability while the much noisier CCD array provides the long term stability. The result is a system that possesses the desirable characteristics of both devices. The combined signal is used to compensate the focal plane image by moving a two-axis steerable mirror in the SIRTF optical system.

The readout and control of the 800x800 element CCD is performed by a small, high performance microcomputer built into the SIRTF onboard electronics. The computer accepts raw video data from the CCD, performs an interpolation algorithm in order to effectively enhance the CCD resolution [8], and generates a pointing error signal for each of the three axes based upon the relationship between the desired and the current positions of the tracked stars in the CCD field of view [9].

Thus, a precise measure is available from the CCD of the current orientation of the telescope optical axis, irrespective of thermal mechanical distortion, or external star tracker alignment. The error signal derived from this measurement is processed by a Kalman filter in the SIRTF microcomputer to correct the gyro outputs; both in pointing offset and drift. The time constant for these error corrections is naturally quite long, on the order of tens of seconds (or hundreds of seconds when tracking M_V+14 stars).

The problem of short-term, high-bandwidth stability is solved by controlling the image with a gimballed mirror which functions as the secondary mirror in the cassegrain optical system of the SIRTF. Using this mirror as an image steering device is a natural application since it already must have a high performance servo system in order to spatially chop the image.

Any motion of the IPS-SIRTF sensed by the gyros, but not corrected for by the IPS controller, will be compensated by moving the steering mirror. The IMC system acts to increase the system bandwidth by acting on disturbances to which the IPS cannot respond. The steering mirror is

driven directly in a feed-forward mode by the IPS gyro outputs. This feed-forward loop provides two important advantages: (1) the bandwidth is limited only by the bandwidth of the gyro and of the mirror servo, not the closed loop system bandwidth of the IPS-SIRTF; and (2) the possibility of a SIRTF structural resonance exciting a control system instability is eliminated since there is no direct closed loop between the sensor and actuator. Feed-forward loops of course are sensitive to errors in scale factor. An analysis of the effects of scale factor error has been performed for this system and will be discussed in a later section.

Figures 1 and 2 are schematic and block diagrams respectively of the IMC system. Note the direct interfaces between the SIRTF microcomputer, the IPS three-axis gyro package, and the steering mirror. The IMC is also coupled to the SIRTF control console in order to provide the operator with a video star field display, control of the telescope optical axis, and CCD operational parameters (e.g., threshold, integration time, and number of tracked stars) [10].

Fig. 1: Schematic of the SIRTF IMC System

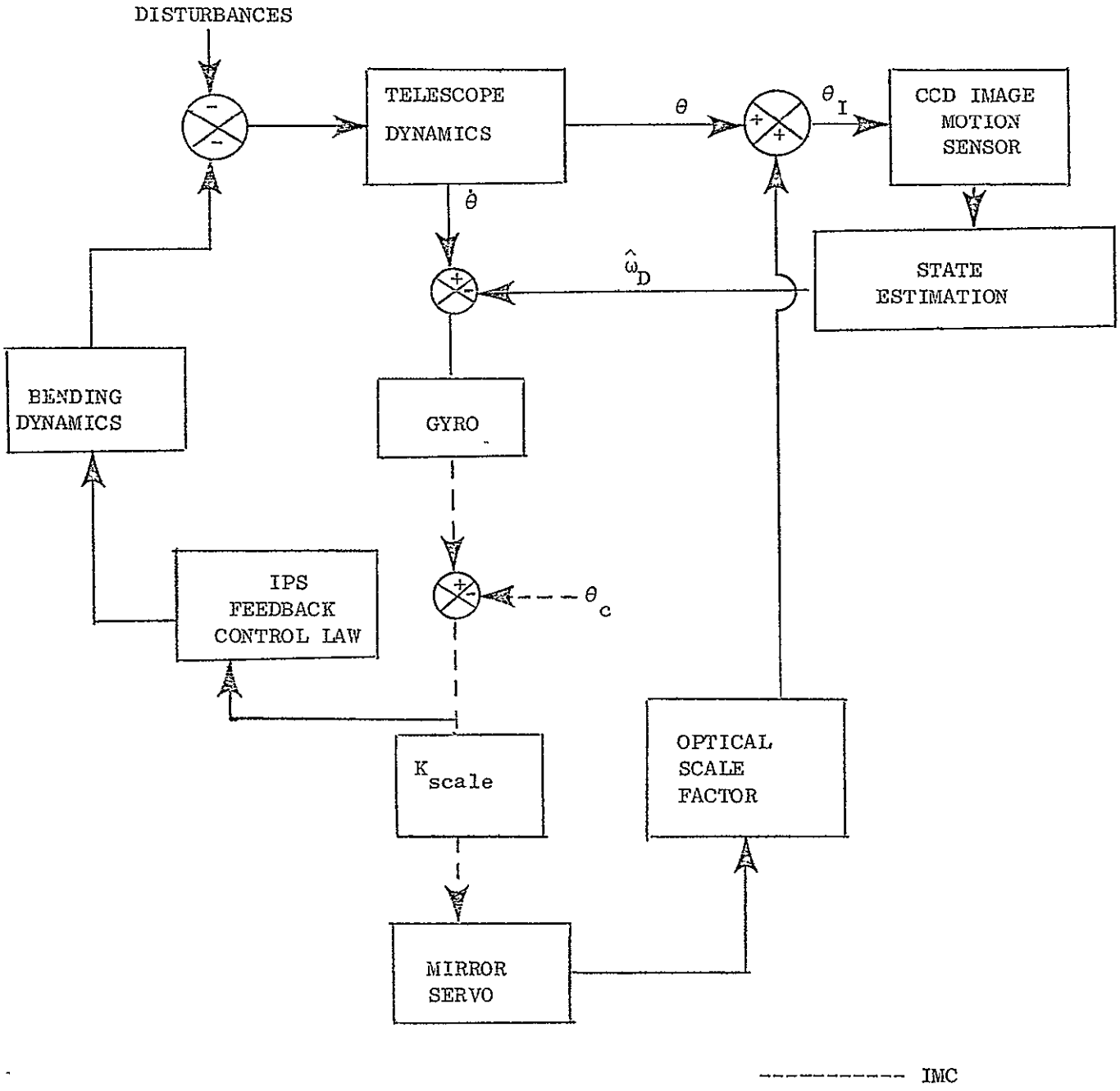

Fig. 2: Block Diagram of the SIRTF/IMC System

III. ANALYSIS OF THE IMAGE MOTION COMPENSATION SYSTEM

A number of system- and environment-related factors were involved in the design and performance analysis of the IMC system. The fundamental problem was one of synthesizing a system that would be insensitive to a variety of noise and disturbance inputs, yet could operate with the limitations imposed by tracking M_v+14 stars.. For the purposes of analysis, the telescope and IPS system were considered to be continuous. Actually, the IPS feedback control law is to be digital with a sample rate of 50 Hz; however, this is considerably faster than the digital state estimation loop which is performed at sample rates as low as 0.1 Hz, and therefore it is reasonable to assume the IPS dynamics to be continuous for analysis of behavior substantially slower than 50Hz.

Once a design concept utilizing a combination of digital and continuous loops had been established, the analysis proceeded along two distinct paths. First, the inspection of the response of the continuous portion of the system to Shuttle disturbance torques, feed-forward scale-factor error, and gyro rate noise, and second, optimization of the discrete portion of the system in order to minimize errors from CCD noise, long-term gyro drift, and thermal distortion. Modeling of the system was done only for the single-axis case; however, accurate numerical data to the greatest extent possible were obtained for all relevant CCD, IPS and Shuttle parameters to make the results realistic and useful.

3.1 Continuous Loop Equations of Motion

The governing equations of motion for the continuous portion of the system are:

$$-J_T\ddot{\theta} = J_T\ddot{\theta}_B + V_B\dot{\theta}_B + K_B\theta_B + M_T r_T a_o \tag{3-1}$$

$$V_B\ddot{\theta}_B = -K_B\dot{\theta}_B + K_I(\theta_g-\theta_c) + K_p\left[\omega_n + \ddot{\theta}-\dot{\theta}_c - \frac{d}{dt}(\theta_c)\right] + K_D\left[\dot{\omega}_n - \frac{d}{dt}(\dot{\theta}_c) + \ddot{\theta}\right] \tag{3-2}$$

$$\dot{\theta}_g = \omega_n + \dot{\theta} - \dot{\theta}_c \tag{3-3}$$

$$\theta_I = \theta + 2\theta_B - 2\theta_M \tag{3-4}$$

$$\theta_M = \frac{K_{scale}}{2} (\theta_g - \theta_c) \tag{3-5}$$

where

a_o	lateral acceleration of pivot (m/sec)
J_T	telescope moment of inertia about pivot = 28175kg-m^2
K_p	IPS proportional feedback = 5.7×10^5 Nm/rad
K_I	IPS integral feedback = 3.42×10^5 Nm/rad-sec
K_B	bending mode stiffness = 2.818×10^8 Nm/rad
K_{scale}	feed-forward scale factor = 1.0, nominally (0.95 for error analysis)
K_D	IPS rate feedback gain = 1.29×10^5 Nm/(rad/sec)
M_T	Telescope mass = 2140 Kg
V_B	bending mode damping=2.818×10^4 Nm/(rad/sec)
r_T	telescope center of mass offset = 2.5 m
$\theta, \dot{\theta}$	IPS gimbal angle and angle rate (rad), (rad/sec)
θ_B	rotational bending error of secondary mirror (rad)
θ_g	Gyro output (rad)
$\theta_c, \dot{\theta}_c$	commanded pointing angle and rate (rad), (rad/sec)
θ_M	commanded mirror angle (rad)
θ_I	image angular position on focal plane (rad)
ω_n	gyro rate noise (rad/sec)

As can be seen from the schematic diagram in Fig. 3, Eq. 3-1 represents the telescope dynamics. Figure 3 also shows the geometric aspects of the bending model. Specifically, the gyro mounting orientation and the CCD focal plane are assumed fixed to each other. Furthermore, since the gimbal is assumed to be massless, the torquer acts instantaneously so that it balances the torque from the spring deflection and damping. This last relation is expressed in Eq. 3-2 with the

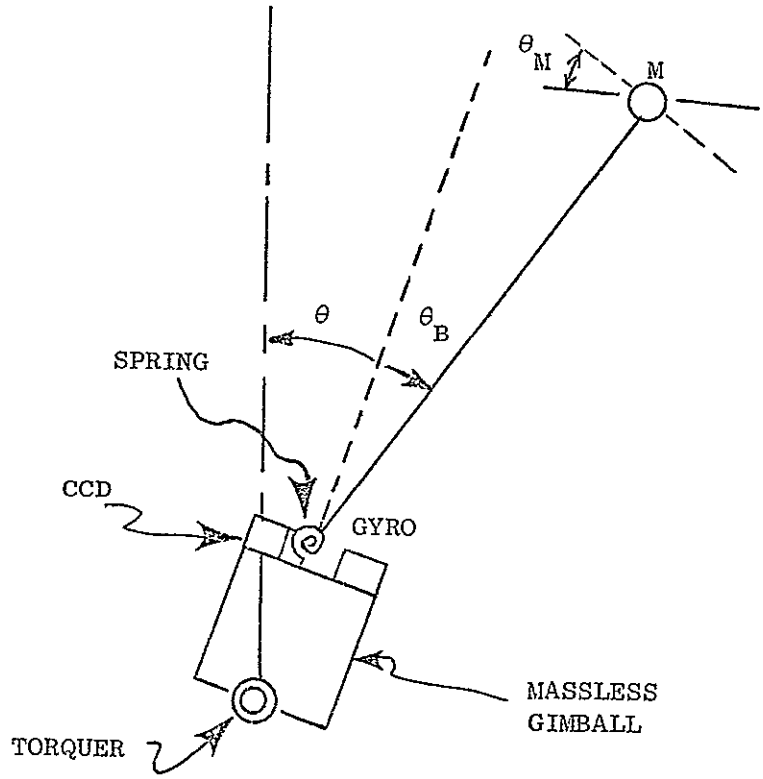

Fig. 3: Telescope/IPS Bending Model
Schematic Diagram

IPS control torque expanded in terms of its components. Eq. 3-4 relates the focal plane image with telescope attitude and mirror attitude changes. It reflects the fact that, with the geometry in Fig. 3, the optical scale factor of the system is 2. It is possible that in the final configuration, the optics may not be structured so that the relation between mirror angle and image motion has this value. Eq. 3-5 reflects this same value (2) of the optical scale factor.

All the equations are contained in the system block diagram shown in Fig. 4.

In the following section, these system dynamics will be used to determine frequency responses to shuttle accelerations and gyro noise. The transfer functions to be used in the frequency response analysis follow directly from Eqs. 3-1 through 3-5 and are:

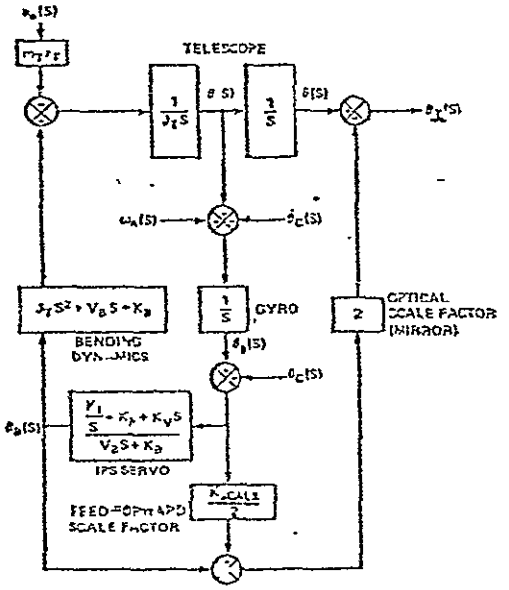

Fig. 4. Block diagram of the continuous portion of the IMC system

Fig. 4· Block Diagram of the Continuous Portion of the IMC System

$$
\begin{bmatrix}
\frac{\theta(s)}{a_o(s)} & \frac{\theta(s)}{\omega_n(s)} \\
\frac{\theta_B(s)}{a_o(s)} & \frac{\theta_B(s)}{\omega_n(s)} \\
\frac{\theta_g(s)}{a_o(s)} & \frac{\theta_g(s)}{\omega_n(s)} \\
\frac{\theta_I(s)}{a_o(s)} & \frac{\theta_I(s)}{\omega_n(s)}
\end{bmatrix}
=
\frac{
\begin{bmatrix}
-\frac{M_T t_T}{J_T} s(V_B s+K_B) & -\frac{1}{s}(K_D s^2+K_p s+K_I)\left(s^2+\frac{V_B}{J_T} s+\frac{K_B}{J_T}\right) \\
-\frac{M_T r_T}{J_T}(K_D s^2+K_p s+K_I) & s(K_D s^2+K_p s+K_I) \\
-\frac{M_T r_T}{J_T} s(V_B s+K_B) & s^2(V_B s+K_B) \\
-\frac{M_T r_T}{J_T}[(1-K_{scale})s(V_B s+K_B) & \frac{1}{s}(K_D s^2+K_p s+K_I) \\
\quad + 2(K_D s^2+K_p s+K_I)] & \cdot\left(s^2-\frac{V_B}{J_T} s-\frac{K_B}{J_T}\right) - K_{scale} \\
 & \cdot s^2(V_B s+K_B)
\end{bmatrix}
}{
(V_B s+K_B)\left(s^3+\frac{K_D}{J_T} s^2+\frac{K_p}{J_T} s+\frac{K_I}{J_T}\right) + s^2(K_D s^2+K_p s+K_I)
}
\qquad (3\text{-}6)
$$

3.2 Discrete Loop Difference Equations

Figure 4 shows the focal plane image as $\theta_I(s)$. The CCD measurement is an average of the image motion over the CCD integration interval, hence if the rate of image motion is assumed constant over one integration interval,

$$\theta_{CCD}(i+1) = \frac{\theta_I(i+1) + \theta_I(i)}{2} \tag{3-7}$$

where θ_{CCD} is the measured value of θ_I from the CCD. Using z-transforms, Eq. 3-7 can be written

$$\frac{\theta_{CCD}(z)}{\theta_I(z)} = \frac{z+1}{2z} \tag{3-8}$$

An approximate transfer function

$$\frac{\theta_{CCD}(\ )}{\theta_I(s)} = \frac{1/T}{s+1/T} \tag{3-8a}$$

models attenuation by the CCD of high frequency image motion.

The image motion compensation system consists of feedforward of gyro measured attitude to the steerable mirror. If there is no scale factor error between gyro measured attitude and the image motion caused by the mirror angle commands, the image motion errors will be solely due to gyro noise and drift and the structural bending that occurs at a higher frequency than the CCD bandwidth. The goal of the discrete compensation system is to estimate gyro error from the CCD measurements. The estimates are used to correct the telescope attitude, image position, and gyro attitude measurement. The controller uses the outputs of a state estimator for the angle error, θ_D, and the drift, D, to form the gyro rate command:

$$\dot{\theta}_c = \frac{1}{T}\theta_D + D \tag{3-9}$$

Within the limitations of scale error and bending the image motion follows the gyro output. Thus, after one integration interval the controlled image position is

$$\theta_{I_{i+1}} = \theta_{D_{i+1}} + \hat{\theta}_{D_i} + \hat{D}_i T \qquad (3\text{-}10)$$

The image response to gyro drift is negative because the integral IPS control causes the telescope to drift so as to null the rate input of the gyro.

Ignoring for now the gyro noise characteristics the dynamic equations for drift, including the control, are

$$\begin{Bmatrix} \theta_D \\ D \\ \theta_{CCD} \end{Bmatrix}_{i+1} = \begin{bmatrix} 1 & T & 0 \\ 0 & 1 & 0 \\ -1 & -T/2 & 0 \end{bmatrix} \begin{Bmatrix} \theta_D \\ D \\ \theta_{CCD} \end{Bmatrix}_i + \begin{bmatrix} -K_g T & -T \\ 0 & 0 \\ K_g T/2 & T/2 \end{bmatrix} \begin{Bmatrix} \hat{\theta}_D \\ \hat{D} \end{Bmatrix}_i$$

$$+ \text{ gyro noise terms} \qquad (3\text{-}11)$$

where $K_g = 1/T$.

The estimate equations reduce to

$$\begin{Bmatrix} \hat{\theta}_D \\ \hat{D} \\ \hat{\theta}_{CCD} \end{Bmatrix}_{i+1} = \begin{bmatrix} 0 & 0 & 0 \\ 0 & 1 & 0 \\ -\frac{1}{2} & 0 & 0 \end{bmatrix} \begin{Bmatrix} \hat{\theta}_D \\ \hat{D} \\ \hat{\theta}_{CCD} \end{Bmatrix}_i + \begin{bmatrix} K_1 \\ K_2 \\ K_3 \end{bmatrix} \left\{ \theta_{CCD_{i+1}} - \bar{\theta}_{CCD_{i+1}} \right\} \qquad (3\text{-}12)$$

where $\bar{\theta}_{CCD_{i+1}} = -\frac{1}{2} \hat{\hat{\theta}}_{D_1}$.

The following transfer functions are derived from the drift and estimate equations above :

$$\frac{\theta_D(z)}{D(z)} = \frac{T}{z-1}$$

$$\frac{\theta_D(z)}{\hat{\theta}_D(z)} = \frac{-1}{z-1}$$

$$\frac{\theta_D(z)}{\hat{D}(z)} = \frac{-T}{z-1}$$

$$\frac{\theta_{CCD}(z)}{\theta_D(z)} = \frac{-(z+1)}{2z} \qquad (3\text{-}13)$$

$$\frac{\hat{\theta}_D(z)}{\theta_{CCD}(z)} = \frac{K_1}{z-K_1/2}$$

$$\frac{\hat{D}(z)}{\theta_{CCD}(z)} = \frac{K_2 z}{(z-1)(z-K_1/2)}$$

$$\frac{\hat{\theta}_{CCD}(z)}{\theta_{CCD}(z)} = \frac{K_3 z - K_1/2}{(z-K_1/2)z}$$

The discrete compensation consists of processing the θ_{CCD} measurements in the estimator (Eq. 3-12) and then combining the state estimates to torque the gyro by Eq. 3-9. Combining these equations in transfer function form results in:

$$\frac{\dot{\theta}_c(z)}{y(z)} = \frac{(K_1 + TK_2)z - K_1}{(z-1)(z-K_1/2)} \qquad (3\text{-}14)$$

where $y = \theta_{CCD}$ + noise.

Figure 5 shows the discrete compensation contained within the dashed lines. The discrete model of the gyro, mirror command to image motion,

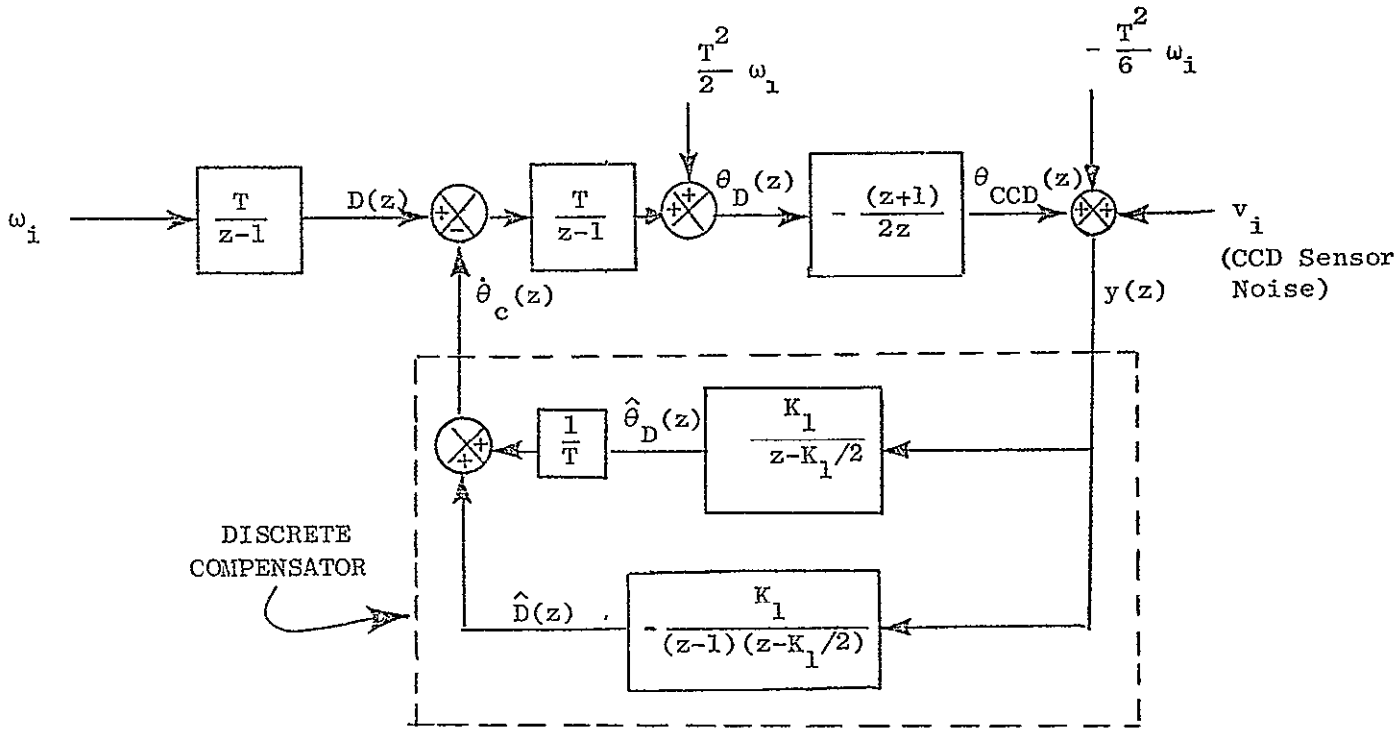

Fig. 5: Discrete Loop Block Diagram

and CCD response are also shown to complete the block diagram for the discrete feedback loop. The noise input, ω_i, provides the discrete equivalent of the long term drift rate and will be described in the following section. An optimal filter which is discussed subsequently also has the form of equation (3-14). The interpretation of the Kalman gains for the optimal filter must be modified because the term $-\frac{T^2}{6}\omega_i$ makes the noise in the measurement y correlated with the random walk driving random sequence. The goal of optimum estimation is minimum variance estimates of drift and drift rate in the presence of sensor noise. Some of the sensor noise characteristics described in reference 10 are summarized below.

3.3 Sensor Noise Model

Gyro noise is modelled as a combination of high frequency rate noise and long-term random walk drift. Characteristics of three candidate Inertial Pointing System gyros are documented in Appendix A of [10] and are summarized in Table I.

Gyro Model	integrated rate noise (arc-sec rms)	random walk drift rate after 1 hr. (arc-sec/sec)rms
Hamilton Standard RI-1139	.11	.01
Bendix 64PM	.11	.0005
Ferranti 125	.017	.0005

TABLE I. Gyro Characteristics

The integrated rate noise is the noise in the image position on the focal plane. This noise is completely transmitted into the angular position of the line of sight by the high bandwidth mirror control. It therefore fundamentally limits the pointing accuracy. High frequency gyro noise is attenuated by the effective CCD transfer function (3-8a) whose break frequency varies inversely with CCD integration time. The resulting r.m.s. noise in the CCD measurement is shown in Fig. 6. These values are generally lower than the intrinsic CCD sensor noise shown in Fig. 7 which is taken from reference 10 and repeated here for completeness. The error covariance of gyro related noise can be obtained from Fig. 6 and added to the CCD sensor noise covariance from Figure 7.

It remains to evaluate the gyro noise terms appearing in (3-11). These are the contribution of long-term random walk drift that is modelled by integrated white noise. The error covariance of the driving white noise is determined so that the r.m.s. random walk drift is equal to the quoted long-term drift after an elapsed time of one hour.

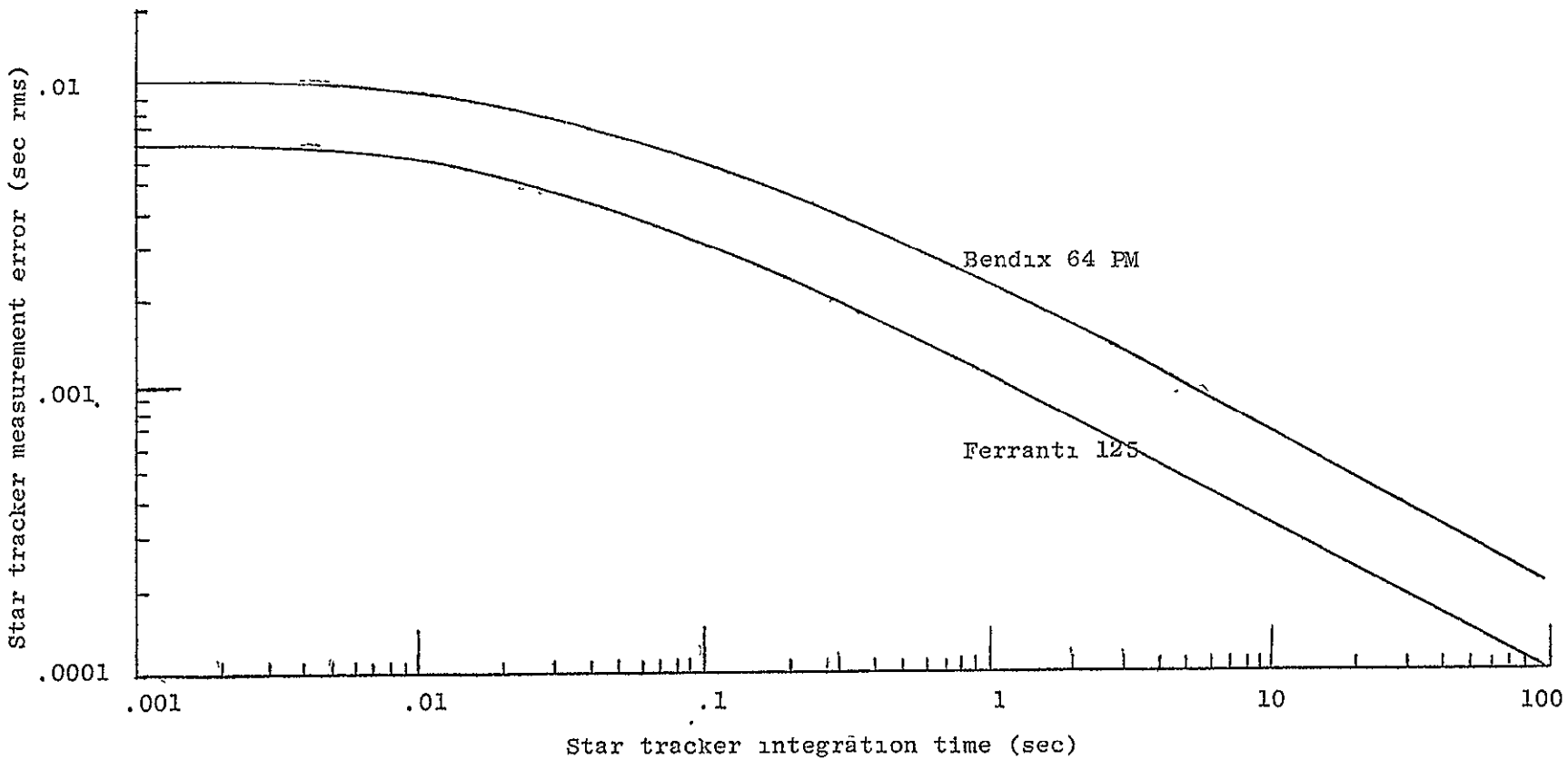

Fig. 6 Star Tracker Measurement Error Resulting From Gyro Rate Noise.

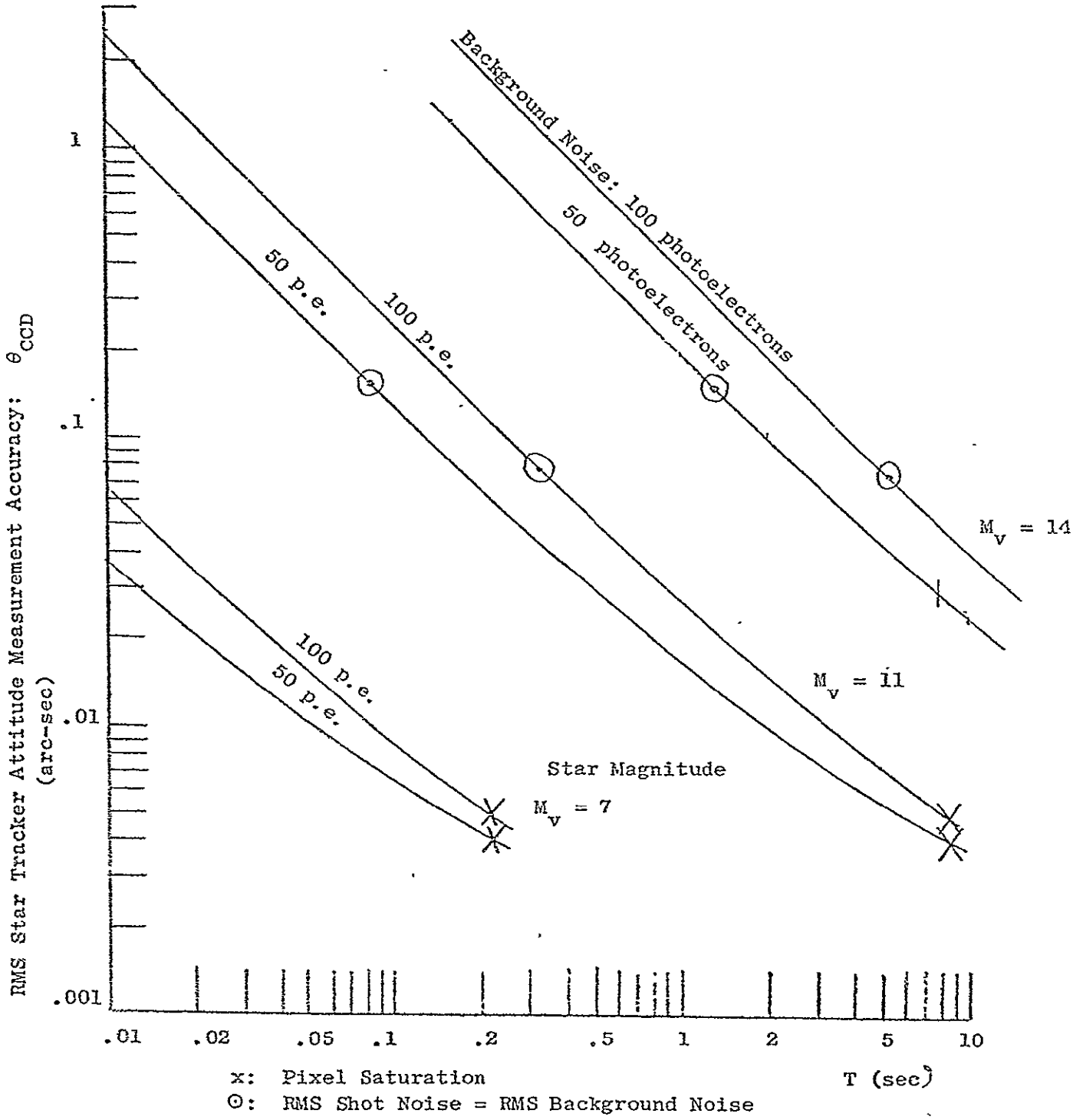

Fig. 7. Sample to Sample Error of Star Tracker Measurement of Image Centroid for a 15 arc-min Field of View (Ref. 10).

The continuous random walk process is modelled by:

$$\dot{D} = \omega \tag{3-15}$$

where D is the random walk drift, and ω is the purely random driving noise. The discrete equivalent of (3-15) is

$$D_i = D_{i-1} + T\omega_i \tag{3-16}$$

The error covariance equation corresponding to (3-16) is:

$$\langle D_i^2 \rangle = \langle D_{i-1}^2 \rangle + T^2 Q$$

or

$$\langle D_i^2 \rangle = \langle D_0^2 \rangle + iT^2 Q \tag{3-17}$$

where i = the i^{th} time interval;
T = the length of the time interval;
$Q = \langle \omega_i^2 \rangle$, and
$\langle\ \rangle$ = an ensemble average of the random variable.

If D_0 is the nominal gyro drift, then using (3-17) over the desired time span of one hour or 3600 seconds:

$$\langle D_{3600/T}^2 \rangle - \langle D_0 \rangle^2 = D_0^2 = \frac{3600}{T} T^2 Q$$

$$\Rightarrow Q = D_0^2/3600T \ . \tag{3-18}$$

The contribution of random walk drift to pointing error is then modelled by

$$\begin{Bmatrix} \theta_D \\ D \end{Bmatrix}_{i+1} = \begin{bmatrix} 1 & T \\ 0 & 1 \end{bmatrix} \begin{Bmatrix} \theta_D \\ D \end{Bmatrix}_i + \underbrace{\begin{bmatrix} K_g T & -T \\ 0 & 0 \end{bmatrix} \begin{Bmatrix} \hat{\theta}_D \\ \hat{D} \end{Bmatrix}_i}_{\text{control}} + \begin{bmatrix} T^2/2 \\ T \end{bmatrix} \omega_i$$

with $Q = \langle \omega_1^2 \rangle$ from (3-18).

It remains to estimate the contribution of random walk driving noise to the measurement $(\theta_{CCD})_i$ in (3-11). The term should model the additional uncertainty in the measurement due to random fluctuations in drift since the previous measurement. If ω_i is constant over any interval, the corresponding image position during the interval is $-\theta_{D_1} - \frac{t^2\omega_1}{2} - D_i t$ where t is measured from the beginning of the interval. The CCD averages the transient component resulting in:

$$\theta_{CCD_{i+1}} = -\theta_{D_i} - \frac{TD_1}{2} - \frac{T^2}{6}\omega_1 \quad . \tag{3-19}$$

The dynamic equations for drift estimation (3-11) become:

$$\begin{Bmatrix} \theta_D \\ D \\ \theta_{CCD} \end{Bmatrix}_{i+1} = \begin{bmatrix} 1 & T & 0 \\ 0 & 1 & 0 \\ -1 & -\frac{T}{2} & 0 \end{bmatrix} \begin{Bmatrix} \theta_D \\ D \\ \theta_{CCD} \end{Bmatrix}_i + \begin{pmatrix} \text{control} \\ \text{term} \end{pmatrix}_i + \begin{bmatrix} T^2/2 \\ T \\ -T^2/6 \end{bmatrix} \omega_i \quad . \tag{3-20}$$

3.4 Design of a Kalman Filter for Drift Estimation

The optimal estimation problem consists of (3-20) together with the measurement equation

$$y_{i+1} = (\theta_{CCD})_{i+1} + v_{i+1} \tag{3-21}$$

where v_{i+1} is the random noise in the CCD measurement. Its expected r.m.s. value is given in Fig. 7.

The open loop transition matrix for this problem is singular and noninvertible due to the fact that it contains a pure delay. However, the inverse is required for solution of the Euler Lagrange equations by eigenvector decomposition [11]. Thus, this efficient numerical algorithm cannot be applied directly. The filter problem can be transformed, however, into one of reduced order to which eigenvector decomposition is applicable.

Equations (3-20) and (3-21) are replaced by the equivalent set

$$\begin{Bmatrix} \theta_D \\ D \end{Bmatrix}_{i+1} = \begin{bmatrix} 1 & T \\ 0 & 1 \end{bmatrix} \begin{Bmatrix} \theta_D \\ D \end{Bmatrix}_i + \begin{bmatrix} -1 & -T \\ 0 & 0 \end{bmatrix} \begin{Bmatrix} \hat{\theta} \\ \hat{D} \end{Bmatrix}_i + \begin{bmatrix} T^2/2 \\ T \end{bmatrix} \omega_i \tag{3-22}$$

$$y_{i+1} = [-1 \quad T/2] \begin{Bmatrix} \theta_D \\ D \end{Bmatrix}_{i+1} - [1/2 \quad T/2] \begin{Bmatrix} \hat{\theta}_D \\ \hat{D} \end{Bmatrix}_i - \frac{T^2}{6} \omega_i + v_{i+1}$$

$$= [-1 \quad -T/2] \begin{Bmatrix} \theta_D \\ D \end{Bmatrix}_i + [1/2 \quad T/2] \begin{Bmatrix} \hat{\theta}_D \\ \hat{D} \end{Bmatrix}_i - \frac{T^2}{6} \omega_i + v_{i+1}$$

The measurement noise is now correlated with the process noise:

$$S = \left\langle \left\{ \frac{T^2}{6} \omega_i + v_{i+1} \right\} \{\omega_i\} \right\rangle \tag{3-23}$$

$$= T^2/6 \quad Q \quad .$$

An equivalent problem in which the process noise and measurement noise are uncorrelated is formed by adding an arbitrary multiple of the measurement equation (homogeneous form) to each state equation:

$$\begin{Bmatrix} \theta_D \\ \dot{D} \end{Bmatrix}_{i+1} = \begin{bmatrix} 1 & T \\ 0 & 1 \end{bmatrix} \begin{Bmatrix} \theta_D \\ \dot{D} \end{Bmatrix}_i + \begin{bmatrix} -1 & -T \\ 0 & 0 \end{bmatrix} \begin{Bmatrix} \hat{\theta}_D \\ \hat{\dot{D}} \end{Bmatrix}_i + \begin{bmatrix} T^2/2 \\ T \end{bmatrix} \omega_i$$

$$+ \begin{bmatrix} L_1 \\ L_2 \end{bmatrix} \left\{ y_{i+1} + [1 \quad T/2] \begin{Bmatrix} \theta_D \\ \dot{D} \end{Bmatrix}_i - [1/2 \quad T/2] \begin{Bmatrix} \hat{\theta}_D \\ \hat{\dot{D}} \end{Bmatrix}_i + \frac{T^2}{6} \omega_i - v_{i+1} \right\}$$

Following the treatment of Bryson and Ho [12], L_1, L_2 are determined so that the modified process noise and measurement noise will be uncorrelated:

$$\left\langle \left\{ \begin{bmatrix} T^2/2 \\ T \end{bmatrix} \omega_i + \begin{bmatrix} L_1 \\ L_2 \end{bmatrix} \{T^2/6 \; \omega_i - v_{i+1}\} \right\} \left\{ -T^2/6 \; \omega_i + v_{i+1} \right\} \right\rangle$$

$$= - \begin{bmatrix} T^4/12 \\ T^3/6 \end{bmatrix} Q - \begin{bmatrix} L_1 \\ L_2 \end{bmatrix} \left(\frac{T^4}{36} Q + R \right) = 0 \quad ,$$

where $R = \langle v_{i+1}^2 \rangle$

$$\Rightarrow \begin{bmatrix} L_1 \\ L_2 \end{bmatrix} = \left(\frac{-T^3 Q/6}{\frac{T^4}{36} Q + R} \right) \begin{bmatrix} T/2 \\ 1 \end{bmatrix} \tag{3-24}$$

Ignoring the measurement and control inputs to the state equations, an equivalent estimation problem can be defined by

$$\begin{Bmatrix} \theta_D \\ D \end{Bmatrix}_{i+1} = \begin{bmatrix} 1+L_1 & T(1+L_1/2) \\ L_2 & 1+TL_2/2 \end{bmatrix} \begin{Bmatrix} \theta_D \\ D \end{Bmatrix}_i + \begin{Bmatrix} \omega_1 \\ \omega_2 \end{Bmatrix}_i \tag{3-25}$$

$$y_{i+1} = [-1 \quad T/2] \begin{Bmatrix} \theta_D \\ D \end{Bmatrix}_{i+1} + v'_{i+1}$$

Measurement and process noise covariances for the equivalent problem are defined by

$$\left\langle \begin{Bmatrix} \omega_1 \\ \omega_2 \end{Bmatrix}_i [\omega_1 \quad \omega_2]_i \right\rangle = \begin{bmatrix} T^2/4 & T/2 \\ T/2 & 1 \end{bmatrix} \left(1 - \frac{T^4 Q/36}{\frac{T^4}{36} Q+R} \right) T^2 Q$$

$$\left\langle \begin{Bmatrix} \omega_1 \\ \omega_2 \end{Bmatrix}_i v'_{i+1} \right\rangle = 0$$

$$\langle (v'_{i+1})^2 \rangle = \frac{T^4}{36} Q + R$$

where

$$\begin{Bmatrix} \omega_1 \\ \omega_2 \end{Bmatrix}_i = \left\{ \begin{bmatrix} T^2/2 \\ T \end{bmatrix} \omega_i + \begin{bmatrix} L_1 \\ L_2 \end{bmatrix} \{T^2/6 \, \omega_i - v_{i+1}\} \right\} .$$

The problem in the form of (3-25) is solved by eigenvector decomposition (DISC program [11]) to obtain the optimal steady state gains $\begin{bmatrix} K_1 \\ K_2 \end{bmatrix}$. The filter is implemented by reintroducing the measurement and control input terms in the estimate equations:

$$\begin{Bmatrix} \hat{\theta}_D \\ \hat{D} \end{Bmatrix}_{i+1} = \begin{Bmatrix} \overline{\theta}_D \\ \overline{D} \end{Bmatrix}_{i+1} + \begin{bmatrix} K_1 \\ K_2 \end{bmatrix} \left\{ y_{i+1} + [1/2 \quad 0] \right\} \begin{Bmatrix} \hat{\theta}_D \\ \hat{D} \end{Bmatrix}_i$$

and

$$\begin{Bmatrix} \bar{\theta}_D \\ \bar{D} \end{Bmatrix}_{i+1} = \begin{bmatrix} L_1/2 & 0 \\ L_2/2 & 1 \end{bmatrix} \begin{Bmatrix} \hat{\theta}_D \\ \hat{D} \end{Bmatrix}_i + \begin{bmatrix} L_1 \\ L_2 \end{bmatrix} (y_{i+1}) \quad , \tag{3-26}$$

which yield

$$\begin{Bmatrix} \hat{\theta}_D \\ \hat{D} \end{Bmatrix}_{i+1} = \begin{bmatrix} L_1/2 + K_1/2 & 0 \\ L_2/2 + K_2/2 & 1 \end{bmatrix} \begin{Bmatrix} \hat{\theta}_D \\ \hat{D} \end{Bmatrix}_i + \begin{bmatrix} K_1 + L_1 \\ K_2 + L_2 \end{bmatrix} (y_{i+1}) \tag{3-27}$$

The z transform of the optimal discrete compensator follows from (3-27) and the control law $\dot{\theta}_{C_i} = \hat{\theta}_{D_i}/T + \hat{D}_i$:

$$\frac{\dot{\theta}_C(z)}{y(z)} = \frac{\left\{\frac{(K_1+L_1)}{T} + (K_2+L_2)\right\} z - \frac{K_1+L_1}{T}}{\left(z - \frac{L_1+K_1}{2}\right)(z-1)} \tag{3-28}$$

The optimal filter has the same form as the compensation (3-14) which results from the standard estimate equations (3-12).

IV. PERFORMANCE OF THE IMAGE MOTION COMPENSATION SYSTEM

The IMC system has been described in Chapter II while the analytical models of the system are contained in Chapter III. This chapter essentially exercises these models, partially with linear analysis tools and partially by numerical simulation, to arrive at performance estimates of the system.

All performance estimates are based on the preliminary SIRTF geometric and dynamic data contained in Fig. 9. The chapter is organized into short term and long term analyses because the techniques used to perform each type of analysis tend to be similar.

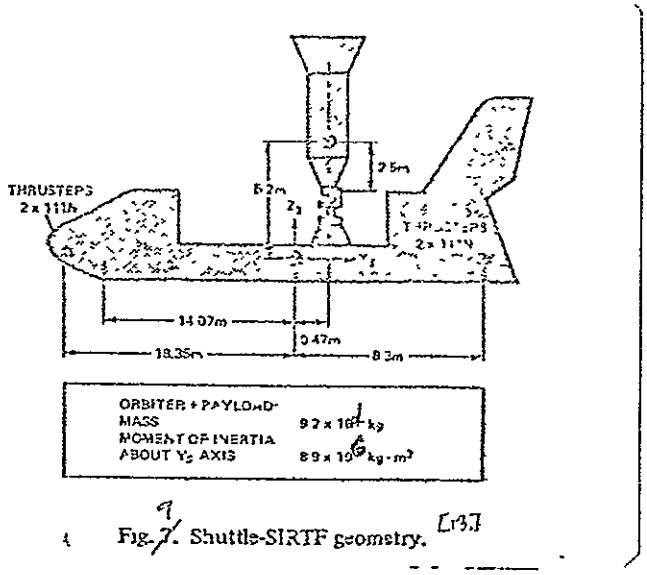

Fig. 7. Shuttle-SIRTF geometry. [13]

Fig. 9 Shuttle-SIRTF Geometry [13]

4.1 Short Term Performance

All but the frequency response results in this section were obtained by the use of a numerical evaluation of the continuous dynamic equations (3-1) through (3-5) and the direct propagation of the discrete equations (3-11). This simulation approach focuses on the response of the system in between updates by the CCD measurements. The frequency response results were obtained by direct evaluation of the transfer functions contained in equation (3-6).

Figure 9 shows the nominal position of the telescope for a single axis simulation about the shuttle pitch axis. The angles of the elevation, cross elevation, and azimuth gimbals are zero.

The steady state response of the gyro output, θ_g, to a constant rate input, $\dot{\theta}_c$, is zero because of the loop integrations; therefore, telescope attitude, θ, drifts in the opposite sense of any gyro drift so as to null θ_g. The transient response of θ reflects the IPS bandwidth while θ_g is equal to the transient deviation of θ from its commanded value. Feed forward of θ_g to the image steering mirror removes IPS transients from the CCD image position to within the assumed feed forward scale error. For purposes of this work, the scale factor error has been assumed to be 5%.

Figure 10 shows the interaction in the frequency domain of the image motion compensation and the 50 r/sec telescope bending mode. The image response to inputs falls off slightly around the IPS bandwidth frequency. Figure 11 shows the significant effect of the feed forward gain accuracy on the image response. Figure 12 shows similar responses to pivot accelerations. In all cases, the telescope and image motion track one another at frequencies below the IPS bandwidth, thus causing the gyro gimbal angle to be very small. As the IPS bandwidth is reached, the telescope ceases to respond, causing the gyro gimbal angle to increase, which is used to command the mirror and maintain the image position at approximately the desired value; the error being essentially equal to the feedforward scale factor error. Although the bending effect produces some error, the perfect scale factor case in Fig. 11 shows this to be very small within the range of interest.

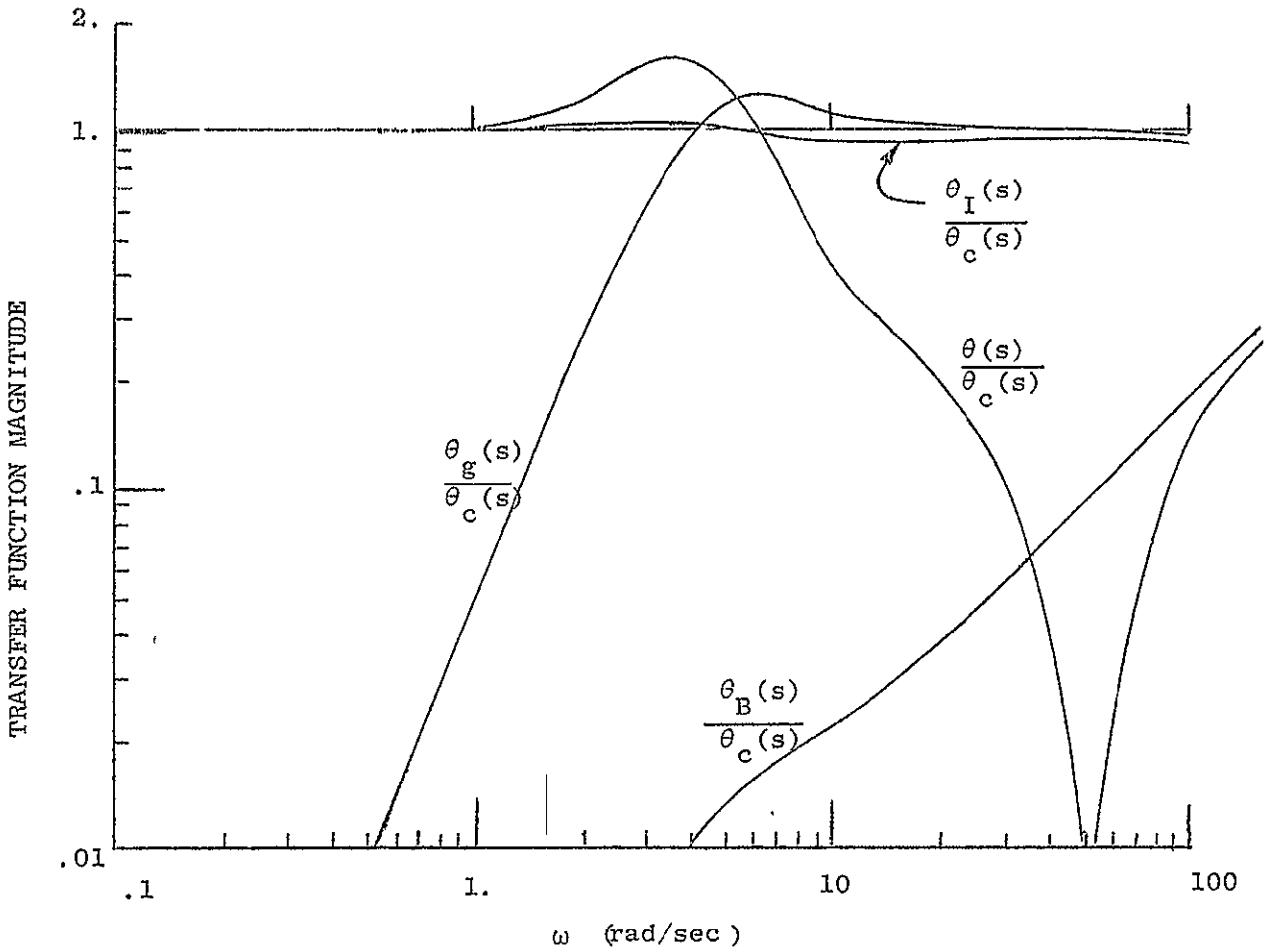

Fig. 10 Magnitude Frequency Response of Image Position to Commanded Attitude, θ_c. (5% foedforward scale error, 50 rad/sec bending mode).

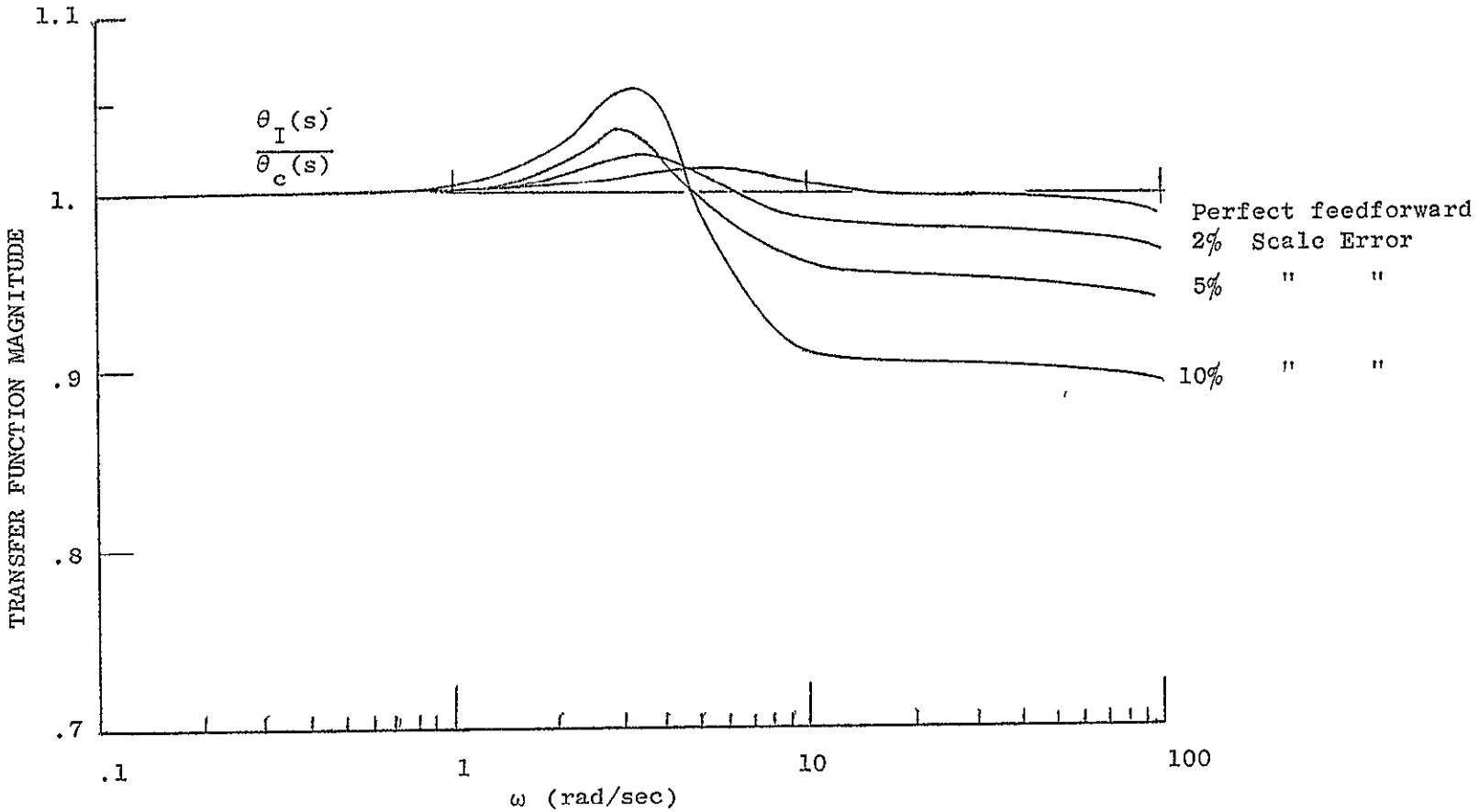

Fig. 11 Magnitude Frequency Response of Image Position to Pointing Commands. (Effect of feedforward scale error in the presence of a 50 rad/sec telescope bending mode.)

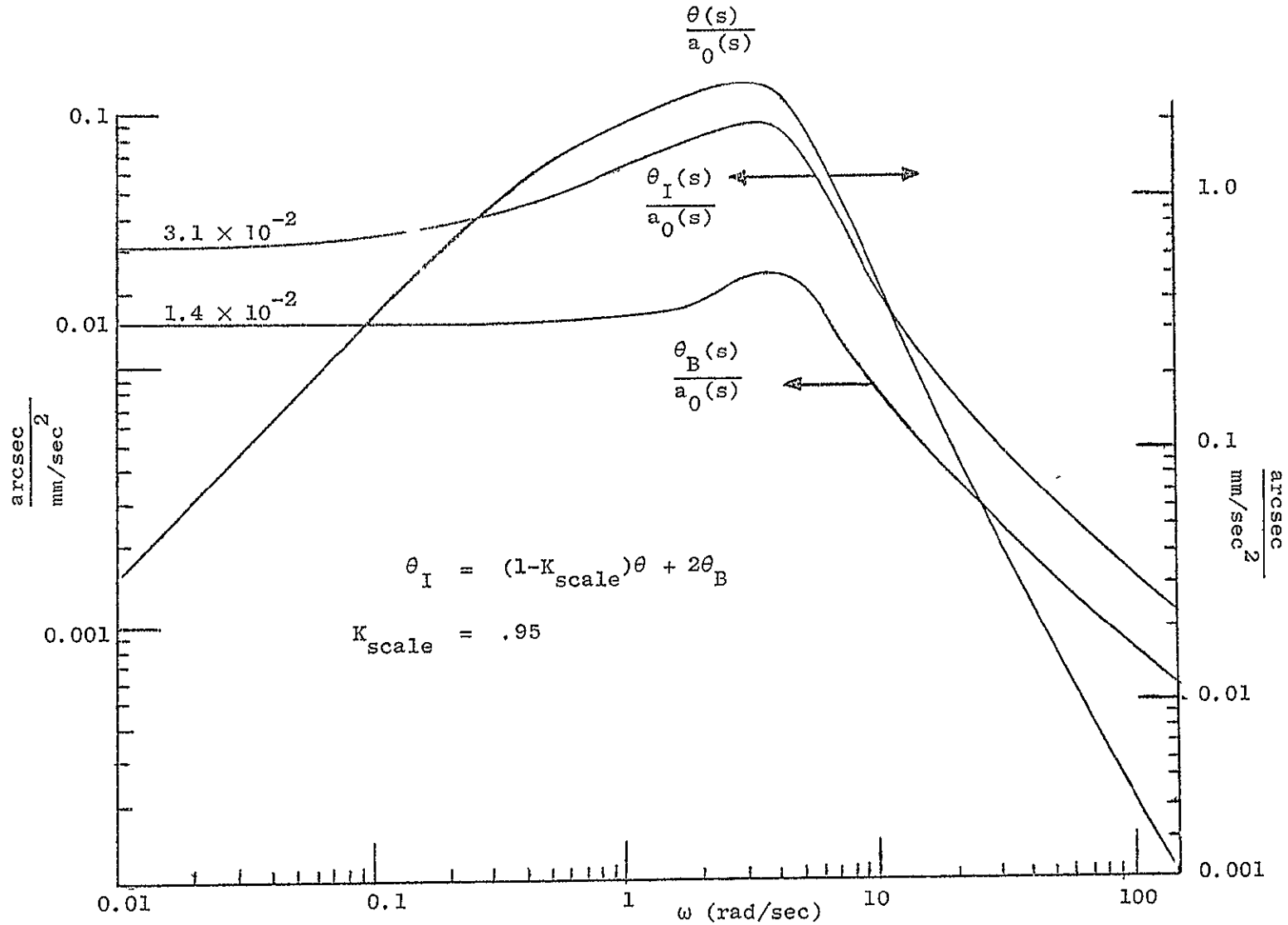

Fig. 12 Magnitude Frequency Response of Image Position to Acceleration a_0 of Telescope Pivot Along Shuttle Roll Axis.

Figure 14 illustrates two shuttle disturbance inputs, an astronaut push-off and the shuttle pitch control limit cycle. The limit cycle consists of $\pm$ .1 deg in attitude and $\pm$ .01 deg/sec in rate [13]. The shuttle accelerations of the gimbal torque the payload whose center of mass is offset from the gimbal.

In the case of a rigid payload the image position responds with the IPS elevation gimbal in proportion to the gyro feedforward scale error. The telescope bending excited by the shuttle disturbance creates an additional component of image position response equal to twice the bending angle. The telescope bending response limits the pointing accuracy that can be obtained in response to disturbances regardless of how accurately the gyro feedforward is scaled.

Figure 15 shows the image position response, θ_I, and the bending contribution θ_B resulting from an astronaut pushoff. These responses are derived by numerical integration of the continuous differential equations (3-1) to (3-5). For the 5% feedforward scale error assumed the image response does not exceed .1 arcsecond. The bending contribution is approximately 30% while the remainder represents the residual of elevation gimbal response, θ, which can be reduced by more accurate feedforward scaling. It should be noted that the θ response shown is for the case where there is no feedforward of the IPS accelerometer measurement. In actuality the feedforward of the IPS base accelerations to the gimbal torquers will directly improve on the accuracy of the IMC alone by reducing both the IPS and bending responses.

The other short term disturbance considered is the action of the Vernier Reaction Control System for the shuttle pitch attitude. The shuttle torque profile of Fig. 14(b) produces accelerations of the elevation gimbal along the shuttle roll axis of 1.8 mm/sec^2 and .6 seconds duration. The accelerations occur in alternating directions every 10.6 seconds and periodically excite short term responses of both the IPS and the payload bending mode. The resulting periodic disturbance of the star tracker image is asynchronous with the star tracker measurement sample times so that the drift estimator response is excited at a beat frequency which is the difference between the limit cycle frequency and the star tracker sample rate.

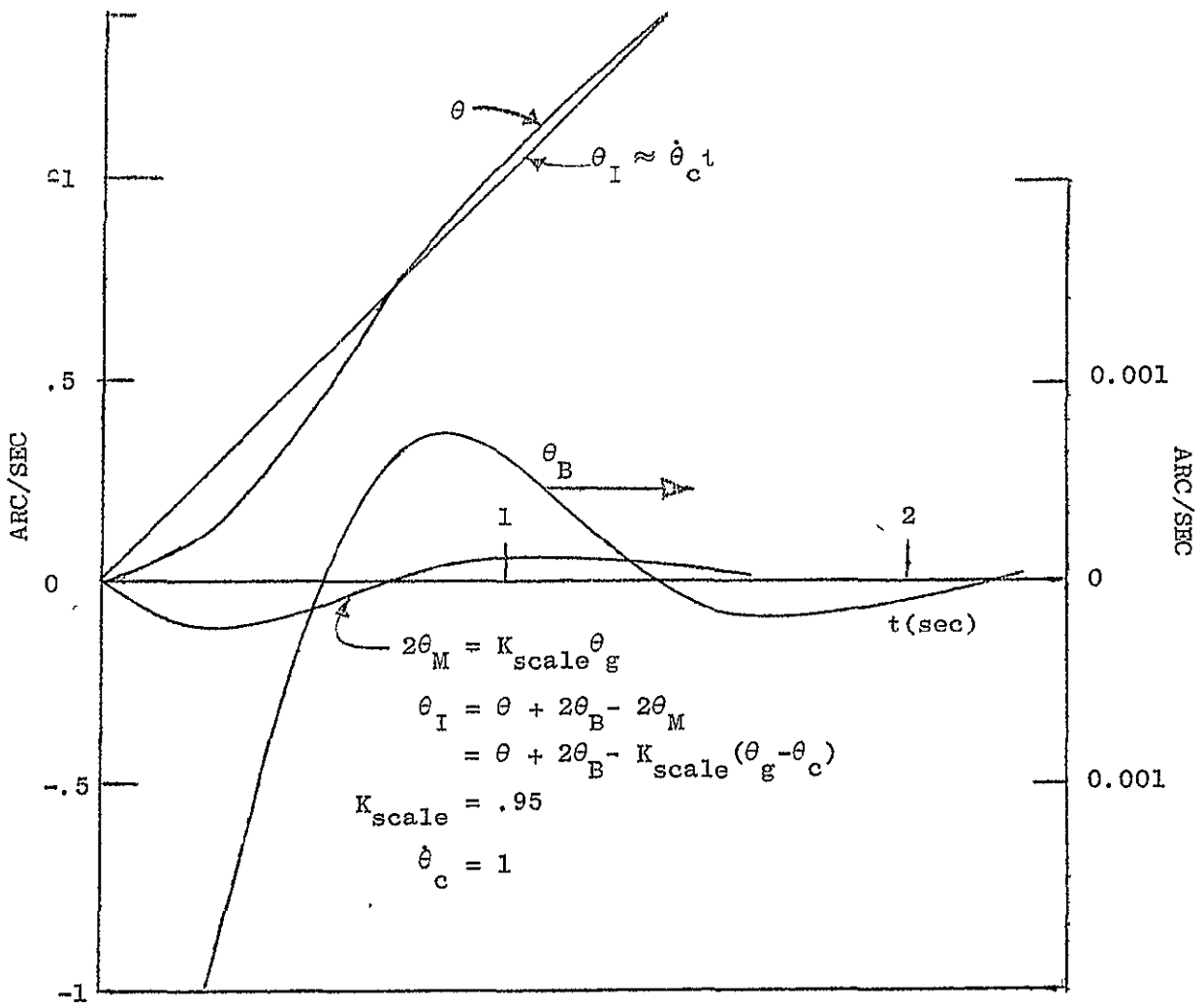

Fig. 13 Response to Step Rate Command.

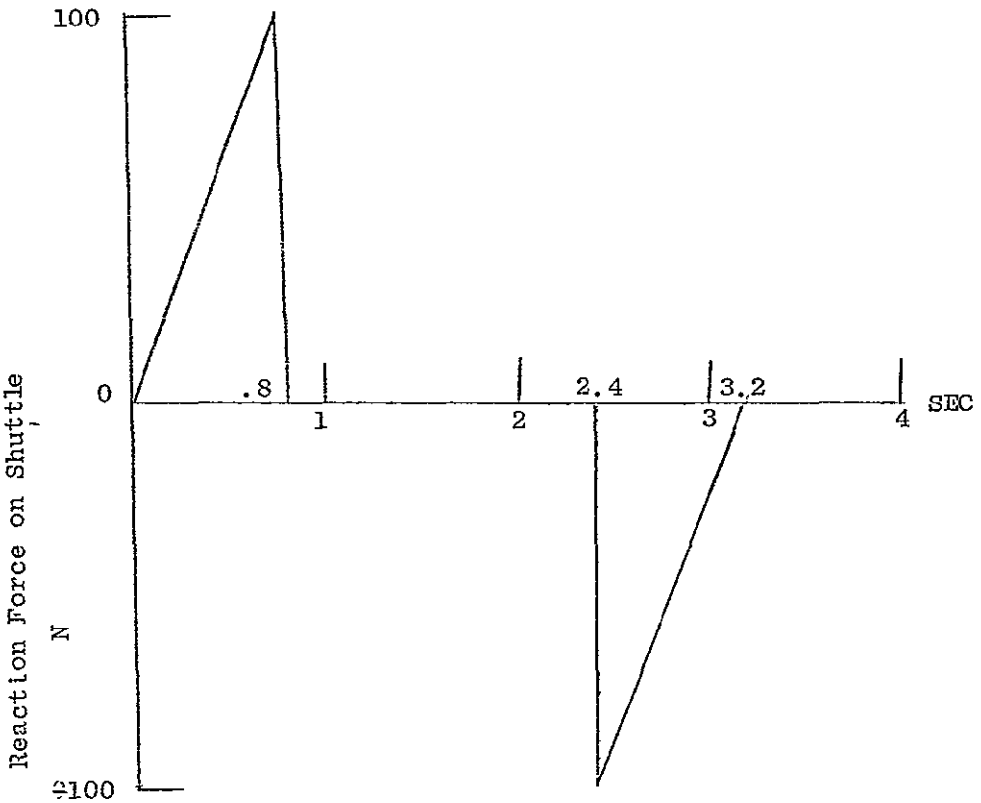

(a) Astronaut Wall Push-Off

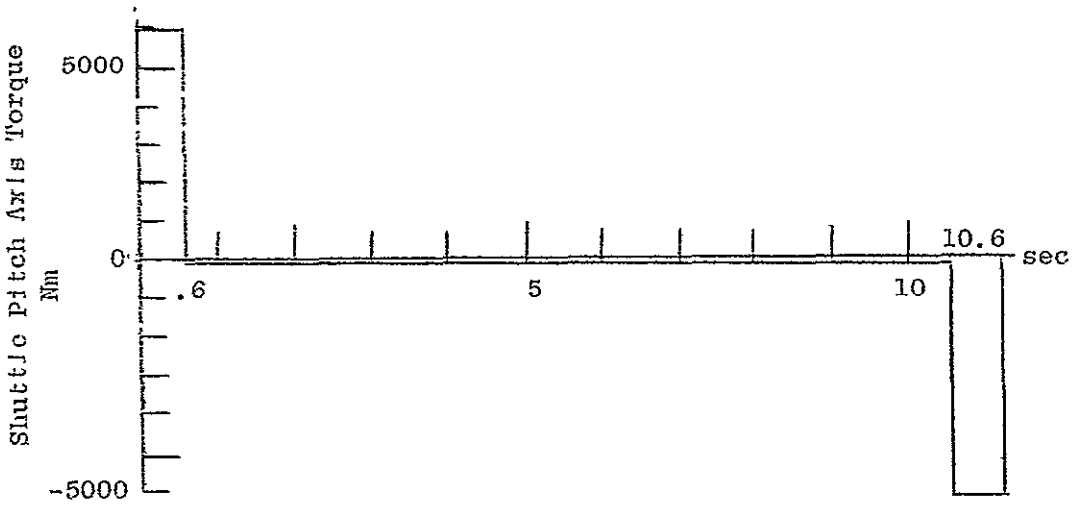

(b) Shuttle Pitch Attitude Limit Cycle

Fig. 14 SHUTTLE DISTURBANCES

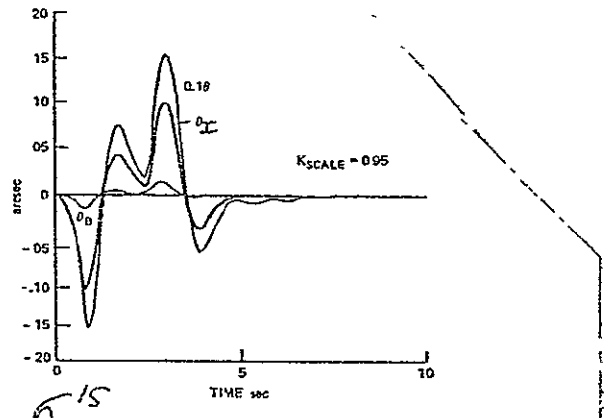

Fig 8. IMC system response to astronaut wall push-off.

Fig. 15 IMC System Response to Astronaut Wall Push-off.

Figure 16 shows the model used to derive the pointing response to the attitude limit cycle. The response of the high sample rate IPS control loop (herein referred to as the "continuous"loop") and the payload bending excitation are calculated by numerical integration of the differential equations (3-1) to (3-5), as in the case of the astronaut pushoff. A fourth order Runga Kutta algorithm and time step of .02 seconds was used for this purpose. The peak image position response in Fig. 17(a) exceeds .2 arcseconds with a 30% contribution from bending. Once again no IPS accelerometer feedforward is assumed.

While a small integration step size is necessary because of the high frequency payload bending dynamics and inordinate amount of computation would be required to generate the digital control loop excitation occurring in response to the attitude limit cycle over relatively long periods of time. Numerical integration is avoided in this case by means of an analysis using a state transition matrix and inverse Laplace transformation.

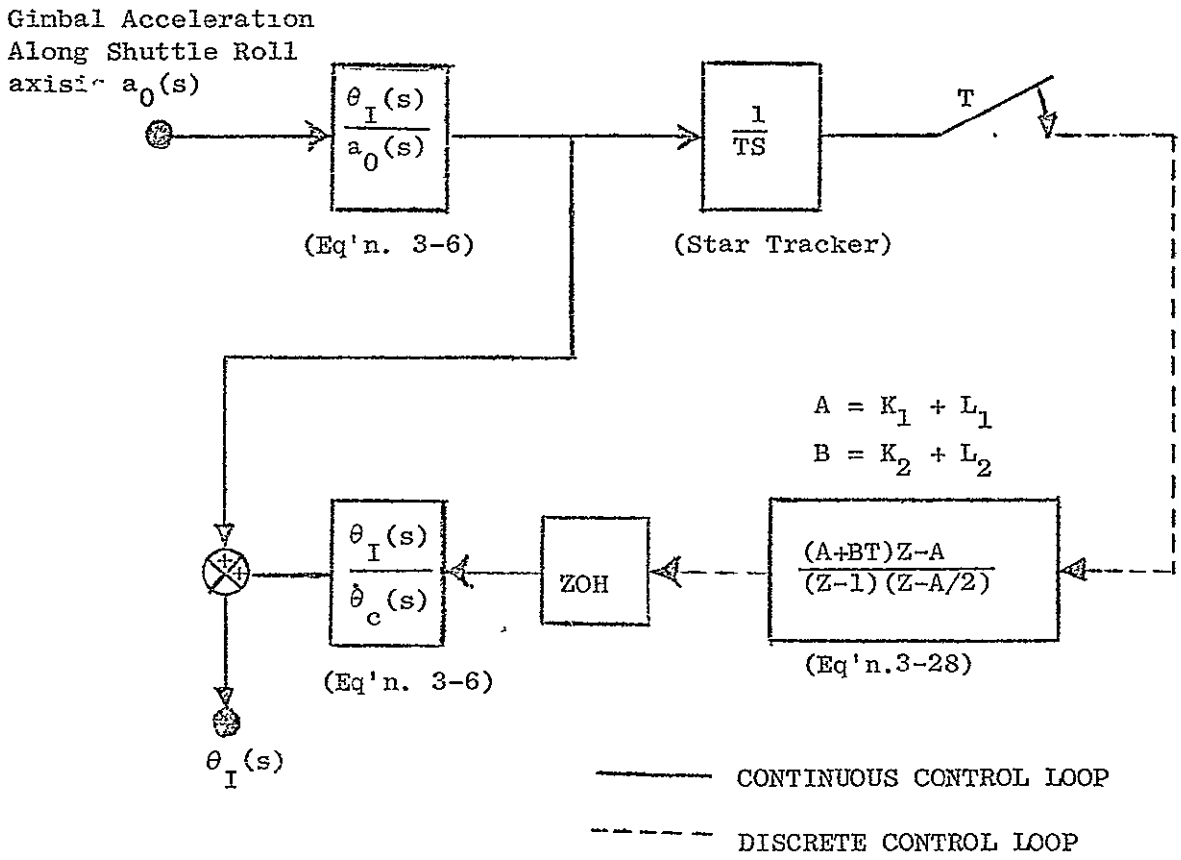

Fig. 16 Simulation Model for Response to Shuttle Limit Cycle

51

Fig. 9 from Carico Lovell et al. report

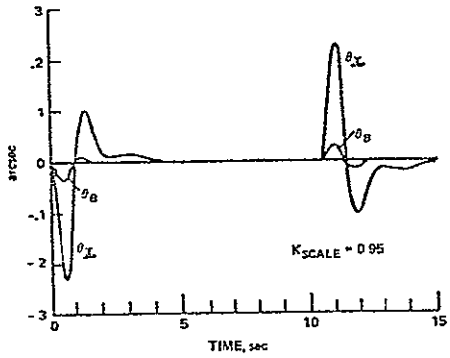

(a) Image Position Response Arising from 5% Feedforward Scale Error and Telescope Bending

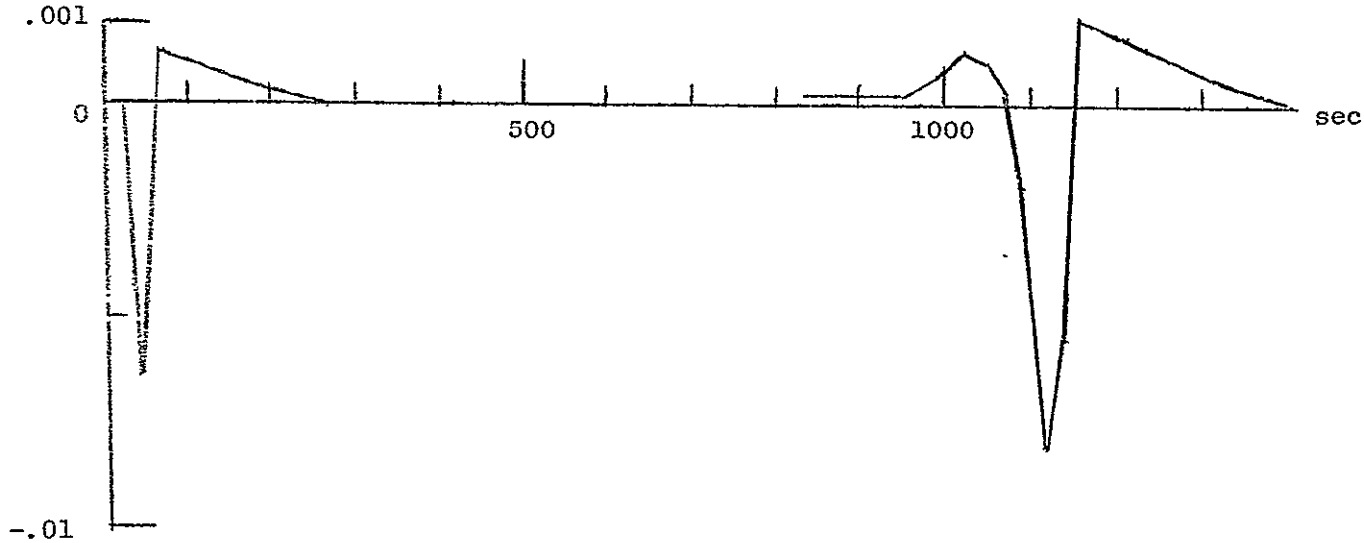

(b) Image Position Response to Discrete Control Action

Fig. 17 RESPONSE TO SHUTTLE PITCH ATTITUDE LIMIT CYCLE.

Figure 17(b) shows the image position response to the digital filter outputs induced by the attitude limit cycle. The filter outputs are in response to the combination of the two image responses shown in Fig. 16. These responses are shown separately to emphasize the large difference in magnitude and time scale between the continuous and discrete loop responses.

The discrete loop response is for a 14^{th} magnitude star filter at a 21 second integration time. This is the sample time which minimizes the drift pointing error for the Ferranti gyro (Table I). The limit cycle period is 21.2 seconds so that two counteracting disturbances occur every filter sample period. The star tracker measurement is not strongly excited as a result and the discrete control activity is not significant in the total image motion. At shorter sample times the star tracker will measure individual thruster disturbances and the discrete loop response will be larger.

4.2 Long Term Performance

Performance of the IMC system over a long term entails the use of a numerical simulation for the cases involving slow transients and the use of linear system covariance analysis for the cases involving steady state response to system noise.

4.2.1 Simulation Description

The long term simulation determines the performance of the digital drift filter and the response to pointing disturbances which are observable by the star tracker. These include gyro drift, gyro feedforward, scale error and mechanical and thermal strains.

In Chapter 3 the star tracker is modeled over many sample periods by a transfer function of $1/TS+1$ (eq'n. 3-8a). This transfer function is used in calculating the contribution of high frequency gyro rate noise to the star tracker measurement error which is a discrete purely random sequence and is uncorrelated with the intrinsic star tracker sensor noise. Its r.m.s. magnitude is given as a function of the star tracker integration time in Fig. 6. Figure 18 is the gyro rate noise model of the IMC system.

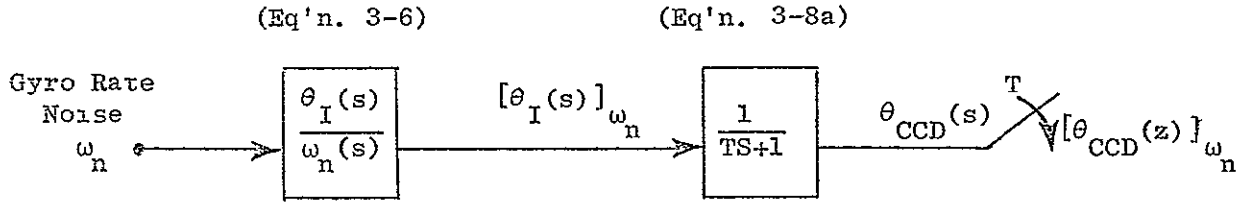

Fig. 18 Contribution of High Frequency Gyro Rate Noise to Star Tracker Measurement.

The purpose of separately modeling rate noise effects is to eliminate the IPS and bending dynamics from the long term simulation. This allows the integration step size to be large. Short term responses show that bending and imperfect feedforward do not significantly affect the response to gyro inputs. The two gyro inputs considered in the long term simulation are random walk drift and digital filter commands. Figure 19 shows the long term simulation model. The image responds perfectly to gyro inputs in this model since feedforward scale error and bending are neglected.

The digital control loop provides attitude rate commands which are the updates of the Kalman filter designed in Chapter 3. These are maximum likelihood estimates of image position based on noisy star tracker measurements. The image is disturbed by random walk variations in drift. The charge coupled device (CCD) in the star tracker must integrate the incident star light for an interval of time before outputting pixel signals. For each different magnitude of star, a particular star tracker integration time and sample period results in the best overall accuracy of drift estimates. The design integration sample time represents an optimum between favorable estimation accuracy for short sample times and favorable star tracker measurement accuracy for long integration times. For the Ferantti model 125 gyro and a 14^{th} magnitude star the r.m.s. drift estimate error is .0093 arcseconds at an optimal sample time of 21 seconds (Table II, Section 4.2.b). The post update estimate error can be further reduced at even longer integration times, but at sample times larger than 21 seconds the closed loop pointing error increases. The closed loop pointing error is shown to be the prior update estimate accuracy in Section 4.2.b.

The heart of the digital control simulation is the digital star tracker simulation of reference [10]. The star tracker model is closely patterned after the actual device. Integration of the incident light intensity is carried out over each pixel and an independent time random noise added to each pixel signal. The geometry of the image and the CCD array are accounted for. Star centroids are determined by the interpolation algorithm described in Appendix A.

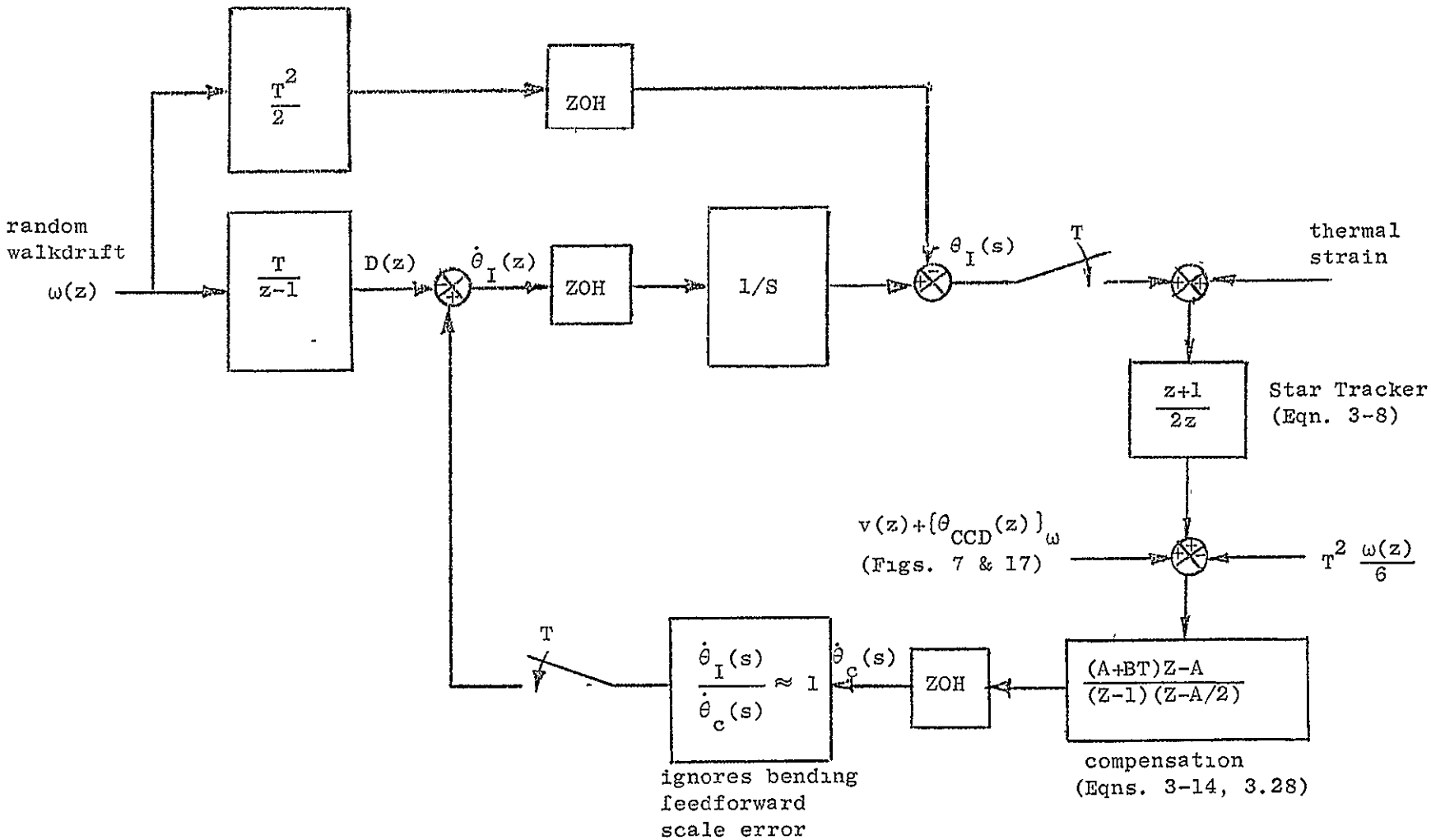

Fig. 19 Long Term Response Model of the Image Motion Compensation System

The actual image intensity distribution formed on the face of the CCD array with image motion is the convolution of the stationary intensity distribution. For the purpose of discrete simulation the image motion is approximated by a uniform rate over each time step. In Fig. 20, I (photons/um^2/sec) is the instantaneous image intensity distribution. $(y',z') = (y,z + Dt)$ define position on the CCD array relative to the initial image position. (y,z) define position relative to the instantaneous image center which is moving uniformly at a rate of D um/sec. The integral with respect to time of the time time-varying intensity at any point is equivalent to an integral with respect to position of the stationary intensity distribution

$$\int_0^{\tau} I(y',z',t)dt = \frac{1}{D}\int_{z'-Dt}^{z'} I(y,z)dz \qquad (4-1)$$

The right hand expression is used for calculating pixel signals in the simulation of the star tracker. Detailed information about the star tracker can be found in reference [10].

It is quite expensive to integrate the image intensity distribution several times during each sample interval. If the image position rate is assumed to be constant over a filter sample period, the star tracker measurement that is obtained by exact simulation is very nearly the average image position. In the simulation responses that follow, the star tracker measurement is modeled as the average of the current image position and the image position at the previous sample time. This allows an order of magnitude reduction in computation time without adversely affecting accuracy. Averaging the image positions is equivalent to modeling the star tracker by the transfer function:

$$\frac{\theta_{CCD}(z)}{\theta_I(z)} = \frac{z + 1}{2z} \qquad (3-8)$$

which has been discussed previously in Chapter 3.

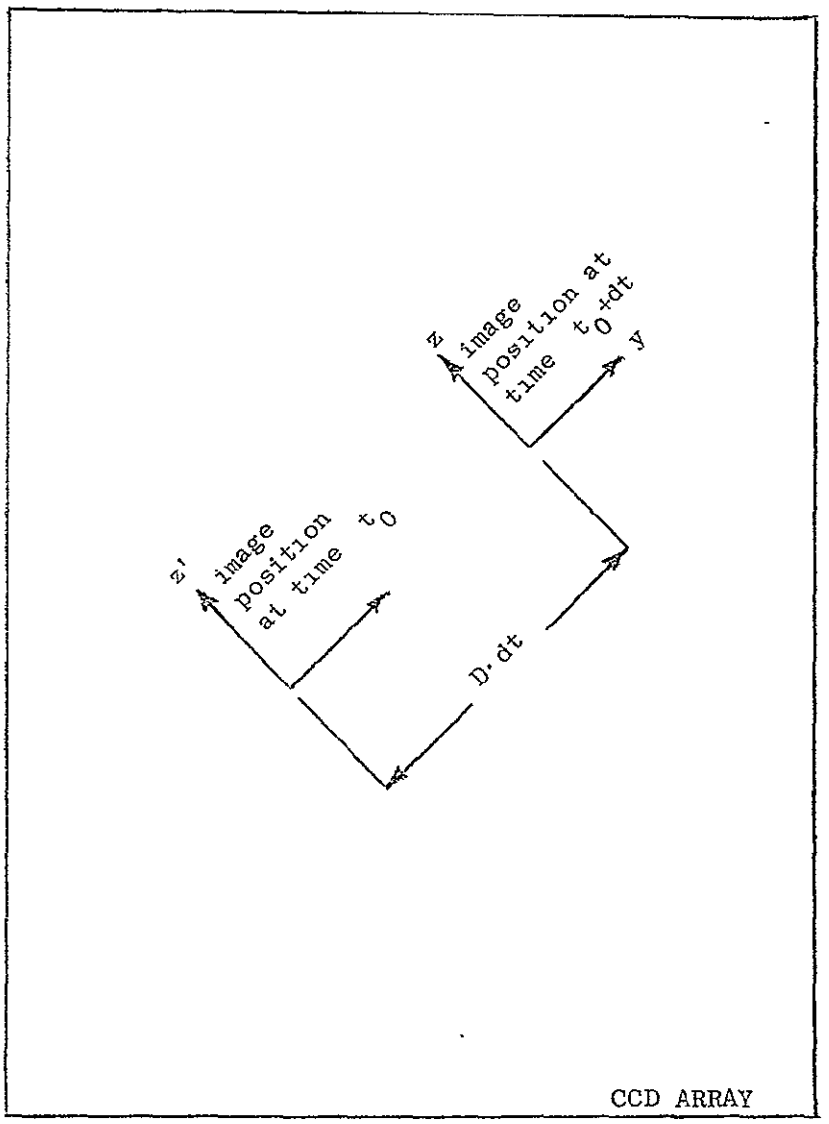

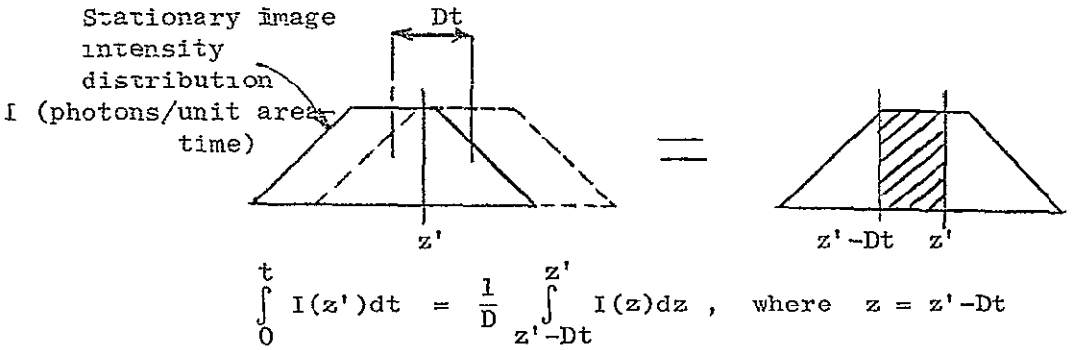

$$\int_0^t I(z')dt = \frac{1}{D}\int_{z'-Dt}^{z'} I(z)dz \quad , \quad \text{where} \quad z = z'-Dt$$

Fig. 20 Interpretation of Intensity Distribution Resulting from Uniform Image Motion as a convolution of the Stationary Intensity Distribution.

4.2.2 Simulation Results for Transient Response

The star tracker noise for a 14^{th} magnitude star measurement is much higher than the Ferranti gyro drift noise. This results in small measurement feedback gains and a slow digital filter transient response. Figure 21 is the image position response for an initial error of -1 arcsec in θ_g and -.1 arcsec/sec in $\dot{\theta}_g$. The image position error increases to 6 arcsec before significant correction to the initial drift rate is provided by the filter. The position error returns to nearly zero in about 10 minutes.

To speed up the slow response to large deterministic image position biases, the filter gains need to be increased In fact a "finite settling" design, which is unique to discrete systems, can null an arbitrary initial state in three sample periods (63 sec), in a highly oscillatory response. In a practical system the finite settling gains could be employed whenever the image position error exceeds a predetermined level. The error will not be nulled exactly because the deterministic image position bias may be slowly changing, and also random sensor noise is present. The finite settling gains will give the best transient response until the response becomes dominated by the sensor noise. After that point the Kalman filter gains are employed because the high finite settling gains only magnify the already high measurement noise. A suitable error level for switching gains is .1 arcsec in the case of 14^{th} magnitude star measurements.

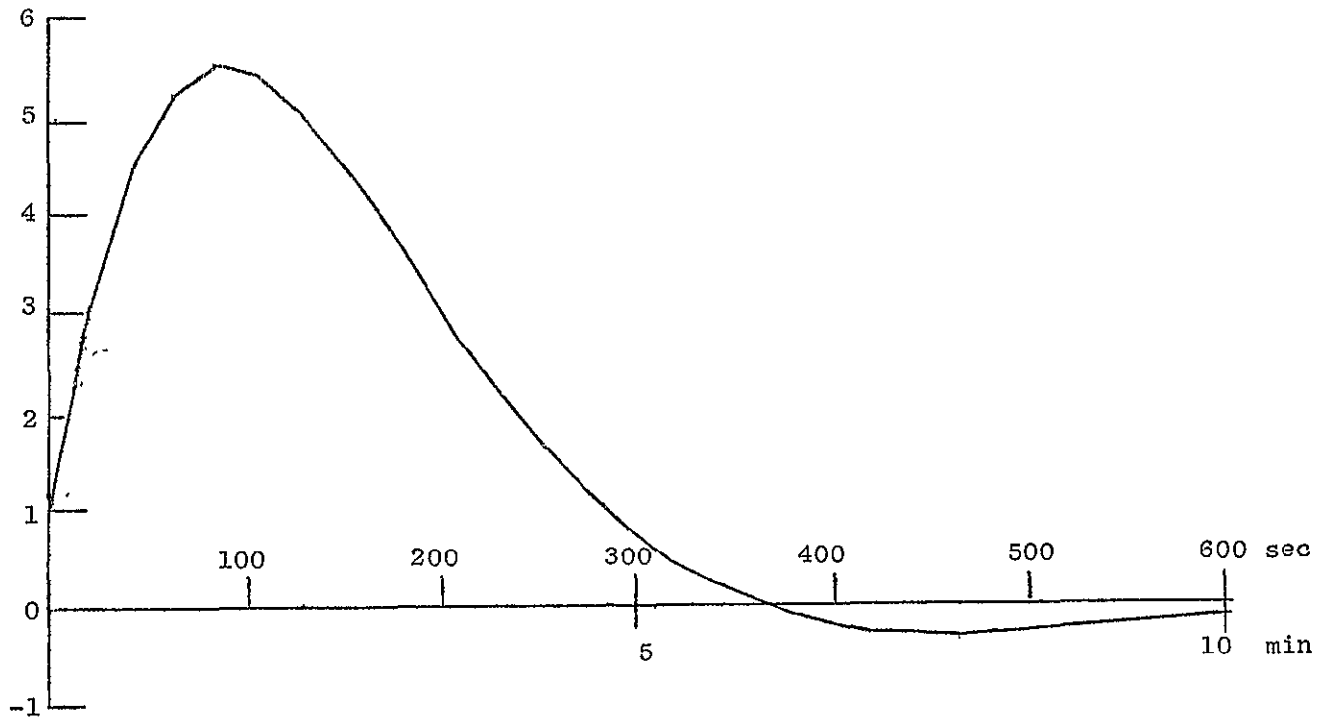

Fig. 21 Image Position Response to Initial Attitude Error of -1 arcsec and Constant Drift Rate of -.1 arcsec/sec Fine Pointing Filter for 14th Magnitude Star, 21 second Integration Time.

4.2.3 Simulation Results for the Thermal Pointing Disturbance

Figure 22 shows a hypothetical pointing disturbance of the telescope which might be caused by a change of the solar illumination incident on the shuttle. The thermal strain transient is characterized by a continuous first derivative, that is, no discontinuities in strain rate. This type of pointing error is not observable by the gyros which undergo no change in orientation. The disturbance of the image is measured by the star tracker, and the filter commands the telescope to an offset position that compensates for the thermal disturbances.

The image response in Fig. 22 is for the 14^{th} magnitude star filter at a 21 second sample time. The digital control is effective in reducing the 60 arcsecond disturbance to a peak error of 2 arcseconds.

4.2.4 Simulation Results for Sensor Noise

The sensor noise inputs in the long term simulation are shown in Fig. 19. The inputs correspond to the noise terms in equations (3-20) and (3-21). The IMC response is simulated for the T = 21 second, 14^{th} magnitude star filter over a period of 2000 samples, or twelve hours. The r.m.s. pointing error is 9.3×10^{-3} arcseconds.

4.2.5 Analytical Drift Estimate Accuracy

Optimal filters are designed using the analysis in Section 3.4 for a 'worst case" 14^{th} magnitude guide star. Star tracker measurement error covariances are determined from Fig. 7 based on a 15 arcmin field of view and 50 photoelectron background noise level.

Figure 23 shows the influence of sample/integration time on the minimum variance drift estimate accuracy. Results are presented for both a Ferantti 125 gyro (comparable to Bendix 64 PM) and a Hamilton Standard RI-1139 gyro.

The telescope may be used in a mode where the steering mirror position is dithered with a square waveform or "chopped." This creates two star images each having an intensity equal to 45% of the intensity developed in a steady image over an equivalent integration interval. The net integration time for a single image becomes .45 times the star

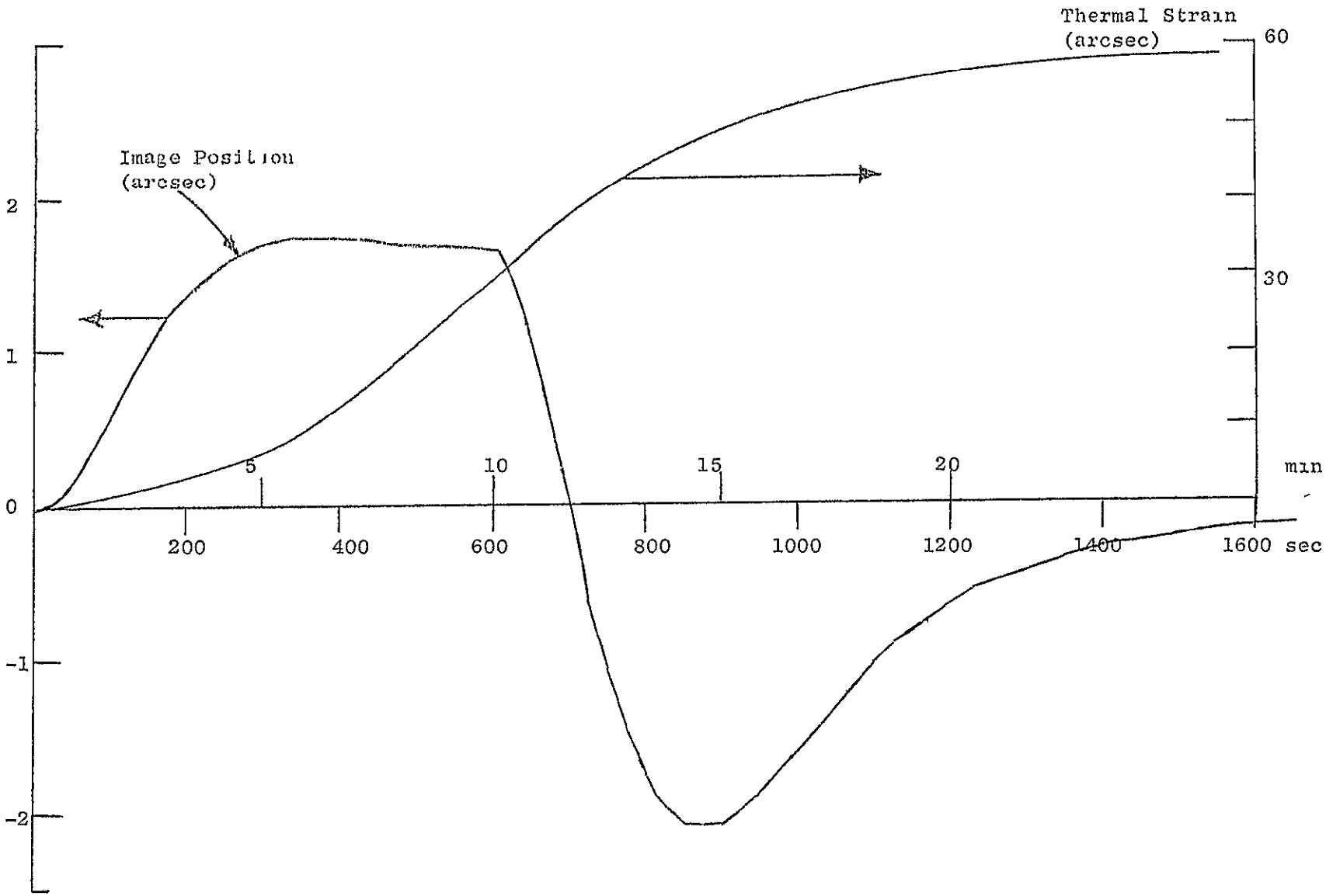

Fig. 22 Response to Thermal Strain with Fine Pointing Filter for 14th Magnitude Star (21 sec integration time).

tracker sample time. The resulting increased measurement noise increases the drift estimate error as shown.

The drift estimate errors presented here are based on perfect centroid determination of the defocused star image on the CCD array. Appendix A discusses the errors of interpolation for chopped and steady images. These errors are reduced to about .02 pixels maximum by use of an appropriate interpolation algorithm. This amounts to a static (non time dependent) error of .06 arcsec in the case of a 15 arcmin field of view.

4.2.6 Analytical Closed Loop Pointing Accuracy in the Presence of Drift

$\theta_{D_{i+1}}$ is the output of the gyro resulting from uncorrected random walk drift. This is the uncorrected error in the image position in the focal plane if there is no scale error in the feedforward of gyro output to the image steering mirror. The r.m.s. pointing error is related to the post measurement update estimate errors by:

$$\theta_{D_{i+1}} = \theta_{D_i} + D_i T - \hat{\theta}_{D_i} - \hat{D}_i T + \frac{T^2}{2}\omega_i$$

$$= -\tilde{\theta}_{D_i} - T\tilde{D}_i + \frac{T^2}{2}\omega_i$$

where

$$\tilde{\theta}_{D_i} \equiv \hat{\theta}_{D_i} - \theta_{D_i}$$

$$\tilde{D}_i \equiv \hat{D}_i - D_i$$

and

$$\langle \theta^2_{D_{i+1}} \rangle = \langle \tilde{\theta}^2_{D_i} \rangle + 2T\langle \tilde{\theta}_{D_i} \cdot \tilde{D}_i \rangle + \langle \tilde{D}^2_i \rangle + \frac{T^4}{4} Q$$

This is precisely the pre-update estimate error. Thus the pre-update error curves of Fig. 23 also give the closed loop pointing error in the presence of drift.

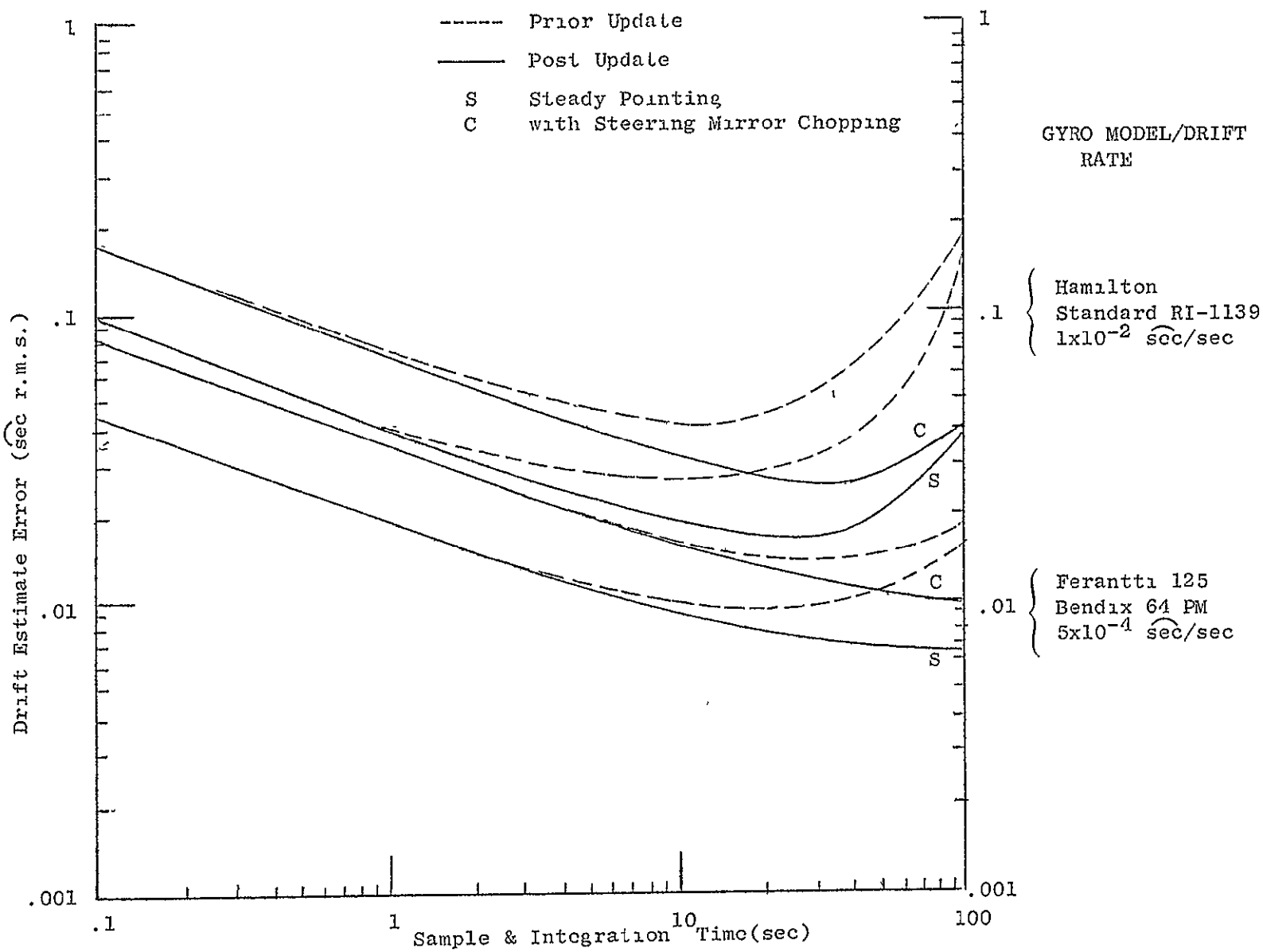

Fig. 23 Drift Estimate Error vs. Sample Time for a 14th Magnitude Star

As can be seen from Fig. 23, there is an optimum sample time which yields the minimum pointing error. This choice of sample time results in the best tradeoff between sensor and process noise. The pointing error remains well within the .1 arcsecond requirement over a wide range of sample times.

Table II summarizes the optimum integration times for the four cases presented and also gives the resulting pointing error for that sample time. It is worthwhile to note that the pointing error of 0.0093 arcsec shown for the steady error with the Ferranti gyro was also predicted by the long term simulation results described in Section 4.2.4. This provides a verification on these two substantially different methods of arriving at the results.

TABLE II

Optimal Sample Times and the Corresponding Minimum Pointing Error

GYRO	Steady Pointing		Chopping		Image Jitter Arising from High Frequency Gyro Rate Noise (arcsec r.m.s.)
	Best Sample Time (sec)	Min Pointing Error $(\text{arcsec})_{rms}$	Best Sample Time (sec)	Min Pointing Error $(\text{arcsec})_{rms}$	
Hamilton Standard RI-1139	10	2.7×10^{-2}	12	4.2×10^{-2}	.015
Bendix 64PM & Ferranti 125	21	9.3×10^{-3}	25	1.4×10^{-2}	.0068

V. CONCLUSIONS

The performance of an image motion compensation (IMC) system for the Shuttle Infrared Telescope Facility, which uses a focal plane CCD star tracker and a steerable mirror, has been analyzed for motion in one axis. The IMC system is necessary because stringent pointing requirements of 0.1 arcsec for SIRTF cannot be met by the shuttle mounted instrument pointing system (IPS). Use of the CCD at the SIRTF focal plane provides gyro offset and drift correction and facilitates a star field display for the SIRTF operator.

Results of the analysis show that the steady state jitter due to gyro and CCD noise is less than 0.02 arcsec for the faintest stars to be used (14th magnitude). This performance can be achieved for steady pointing and while chopping. It assumes that a gyro is used with drift performance equal to that of the Ferranti or Bendix 64PM for the IPS. Furthermore, these pointing stabilities are achieved with CCD integration times between 4 and 100 secs with the best results (0.01 arcsec) at a 21 second integration time.

To obtain the results above, the CCD error model was exercised for both the steady pointing and the chopping case. The interpolation error was essentially unchanged by the chopping and was approximately 0.06 arcsec (with a 15 arcmin field of view) for both cases. However, due to the fainter image while chopping, the total CCD error was approximately doubled for this case.

Results of the transient analysis show that the IMC system attenuates much of the shuttle disturbances on focal plane image motion. Specifically, an astronaut wall push-off produces a maximum image motion excursion of 0.1 arcsec for a feedforward scale factor error of 5%. Shuttle attitude control limit-cycles produce image motion of $\pm$ 0.23 arcsec for a scale factor error of 5%. An 8 Hz bending mode was included in this analysis and accounts for approximately 30% of these transient errors. The remainder is due to the scale factor error and can be reduced by improving the scale factor accuracy. This analysis assumes there is no accelerometer feedforward incorporated in the IPS. In fact, this improvement in the IPS will likely be incorporated. Therefore, to reduce image motion

during shuttle limit cycles to less than 0.1 arcsec, either the gyro/mirror feedforward scale factor need be accurate to 1%, or the combination (product) of the IPS accelerometer feedforward scale factor and the gyro/mirror scale factor need be accurate to 1%. This last case should be easily achievable.

Although a simple bending model was chosen for the analyses above, its frequency (8 Hz) was selected lower than will likely be the case in the final design and therefore its effect is likely larger than will ultimately be the case. With this conservative assumption, bending was found to have no effect on steady state jitter and the small effect on the transient response discussed above.

REFERENCES

[1] Fazio, G.G. (1978) "IR Astronomy Zooms to Prominence," Astronaut. and Aeronaut., Jan. 1978, pp. 40-51.

[2] Lee, G.K. (1978). "Video Inertial Pointing System Software Documentation," Technical Note 1335-53-4, Informatics, Inc., Palo Alto, Calif., pp. 27-29.

[3] Lorell, K.R., J.P. Murphy and C.D. Swift (1976). "A Computer-Aided Telescope Pointing System Utilizing a Video Star Tracker," VII IFAC Symposium on Automatic Control in Space, Rottach-Egern, FRG, May, 1976.

[4] McCarthy, S.G. (1976). "Shuttle Infrared Telescope Facility Preliminary Design Study," Final Report, Hughes Aircraft Co., Culver City, pp. 3-59 to 3-98.

[5] Murphy, J.P., K.P. Lorell and C.D. Swift (1975). "A Computer-Aided Telescope Pointing System Utilizing a Video Star Tracker," NASA TM-X-73,079, pp. 12-14.

[6] Powell, J.D. and A.J. Throckmorton (1975). "A Study of Filter Mechanizations for the Video Inertial Pointing System Microprocessor," Guidence & Control Lab., Dept. of Aero/Astro, Stanford University Final Report, Stanford, CA.

[7] Salomon, P.M. and W.C. Goss (1976), "A Microprocessor-Controlled CCD Star Tracker," 14th Aerospace Sciences Meeting, AIAA, Wash., D.C., Jan. 1976.

[8] Witteborn, F.C. and I.S. Young (1976). "A Cooled Infrared Telescope for the Space Shuttle -- the Shuttle Infrared Telescope Facility (SIRTF)," AIAA Paper 76-174, 21st Annual Meeting of the Amer. Astronaut. Soc., Denver, Aug. 1975.

[9] Young, I.S., F.C. Witteborn and M.K. Kiya (1978). "Shuttle Infrared Telescope Facility Interim Report," Appendix B3, Ames Research Center, NASA, Moffett Field, Calif.

[10] Powell, J.D. and E.K. Parsons (1978). "Control System Concepts for the Shuttle Infrared Telescope Facility," Guidance & Control Lab., Dept. of Aero/Astro, SUDAAR Report No. 510, Stanford Univ., Stanford, CA.

[11] Katz, P. and J.D. Powell (1974). "Selection of Sampling Rate for Digital Control of Aircrafts," Guidance & Control Lab., Dept. of Aero/Astro, SUDAAR Report No. 486, Stanford University, Stanford, CA.

[12] Bryson, A.E. and Y.C. Ho (1975). Applied Optimal Control, Hemisphere Publishing Corp., Washington, D.C., 1975 (Sect. 13.5).

[13] Dornier System Document, IPS-DS-TN-0094.

[14] Final Report 760-175 for Flight Demonstration Model Star Sensor, Jet Propulsion Lab., Pasadena, CA, May, 1977.

[15] Marx, H.B. (1975). "Optimal Coupling of Star Image Characteristics with Algorithm Form for an Accurate Interelement Star Position Determination," Jet Propulsion Lab. Memorandum 343-8-75-510, Pasadena, CA.

[16] Marx, H.B. (1975). "Image Characteristics of the Zenith 130mm Catadioptric Lens as Affected by Defocus and Lens Temperature," Jet Propulsion Lab. Memorandum 343-8-75-732, Pasadena, CA.

[17] Fairchild CCD 211 Preliminary Data Sheet, March 1976.

Appendix A

STAR TRACKER INTERPOLATION ERROR

The face of the CCD detector is divided into a rectilinear pattern of discrete photosensitive elements. Each element integrates the incident light intensity by the accumulation of the photoelectrons which are excited. The location of each photosensitive element is uniquely specified so that it is possible to obtain the precise coordinates within the resolution of the element array of any stars being imaged on the surface of the CCD. The current state of the art for CCD's is an array of 400 elements square. Thus even the most advanced units cannot obtain resolution better than .2 arcseconds for a 15 arcminute field of view.

It is possible through a process of interpolation to extend the resolution by more than an order of magnitude. The star image is defocused into an intensity distribution over a four by four matrix of elements. The center of charge is then computed resulting in an image centroid location within an individual pixel.

Static errors of interpolated star positions interact strongly with the shape of the defocused image. As a defocused image moves around on the array, the error of the interpolated image center and the total signal level fluctuate. These effects are largely caused by the opaque registers which are columns of photosensitive elements in the Fairchild 211 CCD. The image shape and size can be adjusted to control total signal modulation, calculation sensitivity to pixel noise, and the centroid error.

The SIRTF focal plane guidance sensor design is unsettled at this time so the Zenith catadioptric optics of the NASA Ames Video Inertial Pointing System are used as a representative optical design [14]. A study by the Jet Propulsion Laboratory [15] shows that a four element interpolation algorithm coupled with an image width of 2.75 horizontal pixel units results in the following favorable measurement characteristics:

i) total signal modulation 1.5%;

ii) minimum collected signal 40%;

iii) worst case sensitivity to pixel noise, .11 elements;

iv) centroid error .06 elements.

A digital computer simulation of the CCD is used to predict interpolation errors. The characteristics of the assumed image intensity distribution conform to the J.P.L. study's recommendations. The assumed image shape, shown in Fig. A-1, is trapezoidal and covers 2.75 pixels in the horizontal direction. Its line spread is formed by integrating the two-dimensional image intensity distribution in one dimension. The line spread for the image assumed in the simulation roughly corresponds to the experimental line spread for a similar size image of the Zenith optics [16] as shown in Fig. A-2.

In the simple center of charge interpolation algorithm the pixel signals S_{ij} are summed row-wise and columnwise to form vertical and horizontal line spreads S_i and S_j:

$$S_i = \sum_{j=1}^{4} S_{ij}$$

$$S_j = \sum_{i=1}^{4} S_{ij}$$

The centroid address in pixels is

$$\hat{k} = \frac{1.5(S_4-S_1) + .5(S_3-S_2)}{S}$$

relative to the matrix center where

$$S = \sum_{i=1}^{4} S_i = \sum_{j=1}^{4} S_j \quad .$$

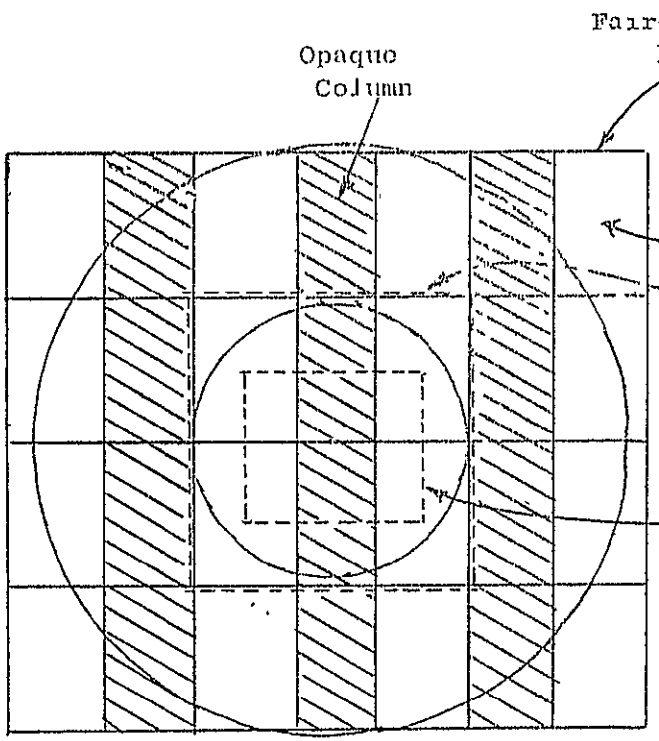

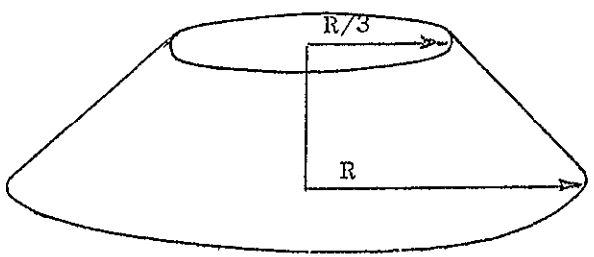

Fig. A-1 Assumed Defocused Star Image Shape and Size Relative to CCD Pixel Matrix.

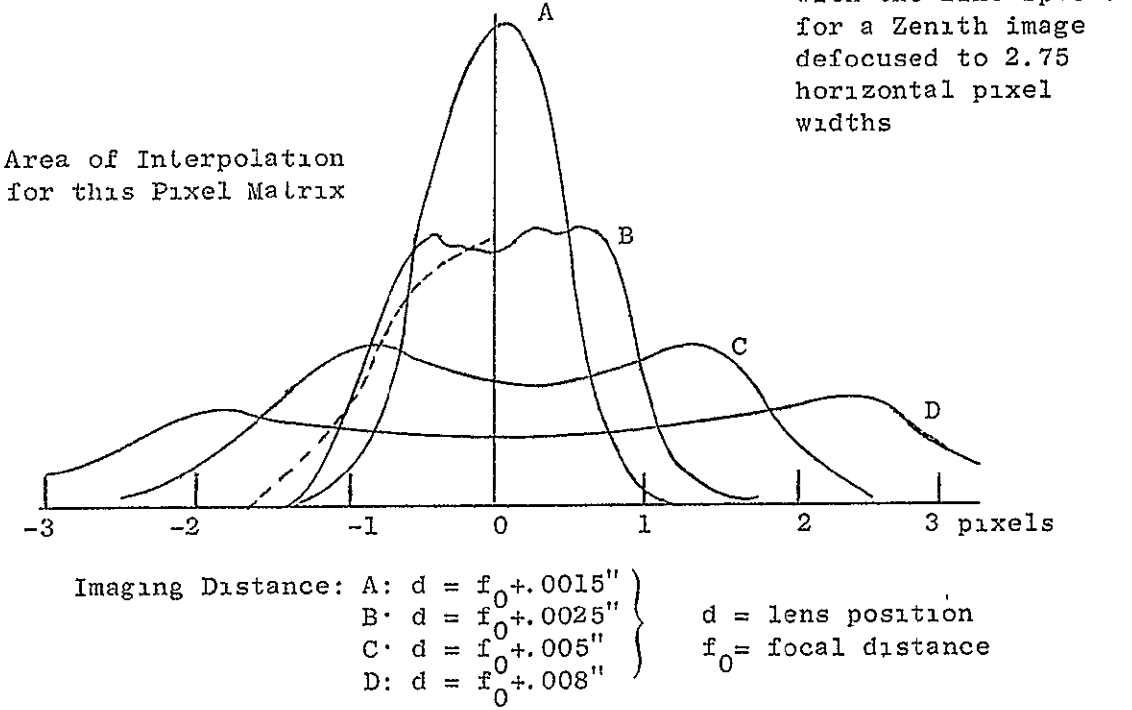

Fig. A-2 Comparison of Line Spreads for a Zenith Catadioptric Lens with Glass Plate with Line Spread for Defocused Image of Fig. A-1.

The above formula is exact only for a uniform intensity line spread and a CCD with no opaque registers. For the nonuniform distribution in Fig. A-1, and the Fairchild 211 CCD physical layout, the following approximate corrections give almost an order of magnitude increase in accuracy:

$$\hat{k}_{vertical} \leftarrow 1.3193\ \hat{k}_{vertical}$$

$$\hat{k}_{horizontal} \leftarrow \pm\ (-.7024 + \sqrt{.4933 + 1.905\left|\hat{k}_{horizontal}\right|}$$

This interpolation algorithm can also be used while the steering mirror is chopping. In the chop mode there are two defocused star images each with 45% of the intensity of a single image. The two images are connected by a faint streaked image along which 10% of the incident intensity is distributed. The intensity of the streaked image is determined from the angular separation of the stationary images which is assumed to be 5 arcminutes.

Figs. A-3 and A-4 show the stationary and streaked images respectively. The intensity of the streaked image is about two orders of magnitude less than that of the stationary image. The effect of the tail on the stationary image interpolation is therefore quite small. Figure A-5 shows the interpolation errors in pixel units for both chopping and steady pointing and their dependence on image centroid position. The maximum centroid error of .017 pixels corresponds to .06 arcseconds in a 15 arcminute field of view. The same interpolation algorithm is used for chopped and stationary images.

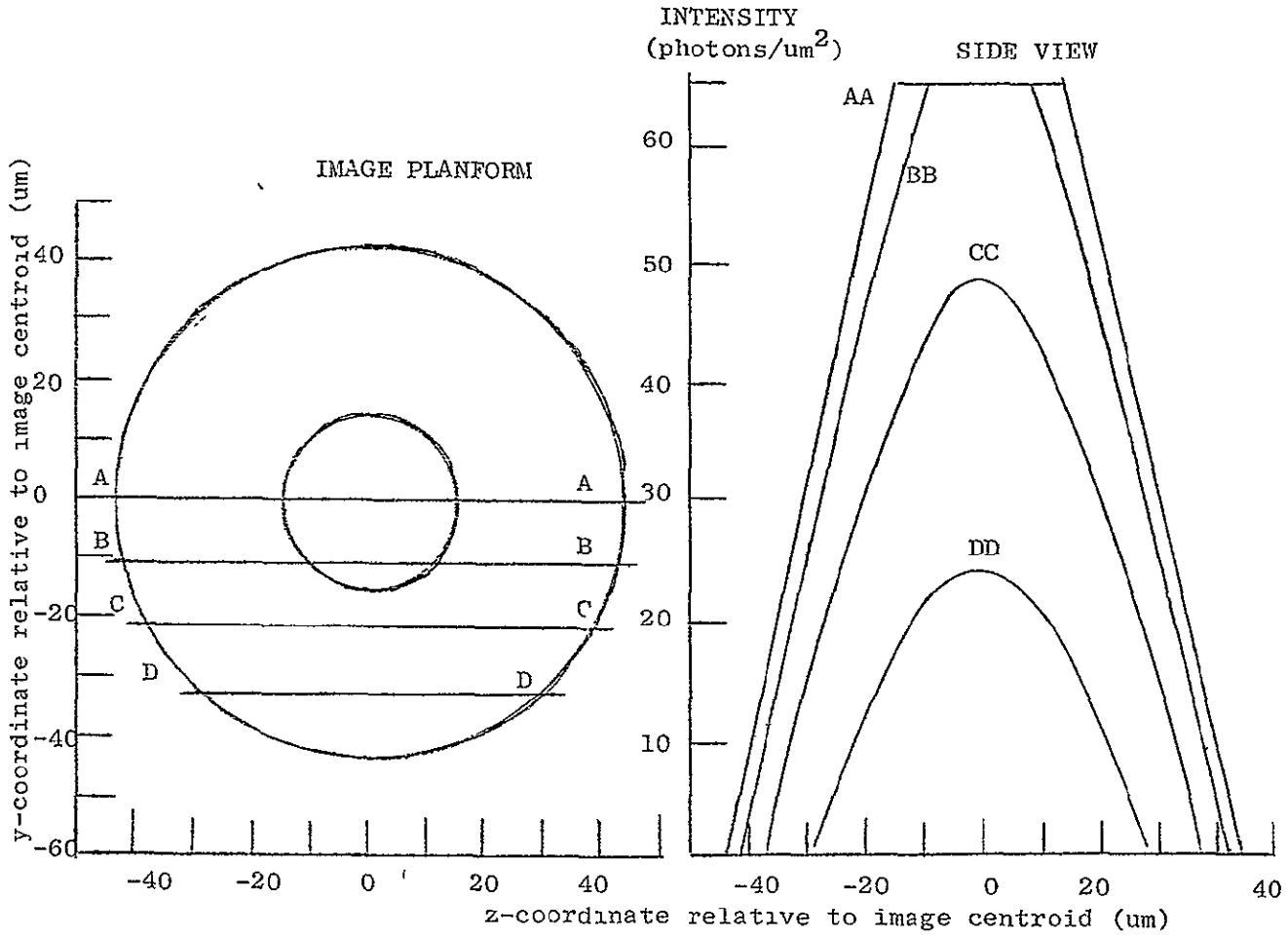

Fig. A-3 Defocused Star Image During 5 arcminute Square Wave Chopping (Integration time 10 sec, 14th magnitude star)

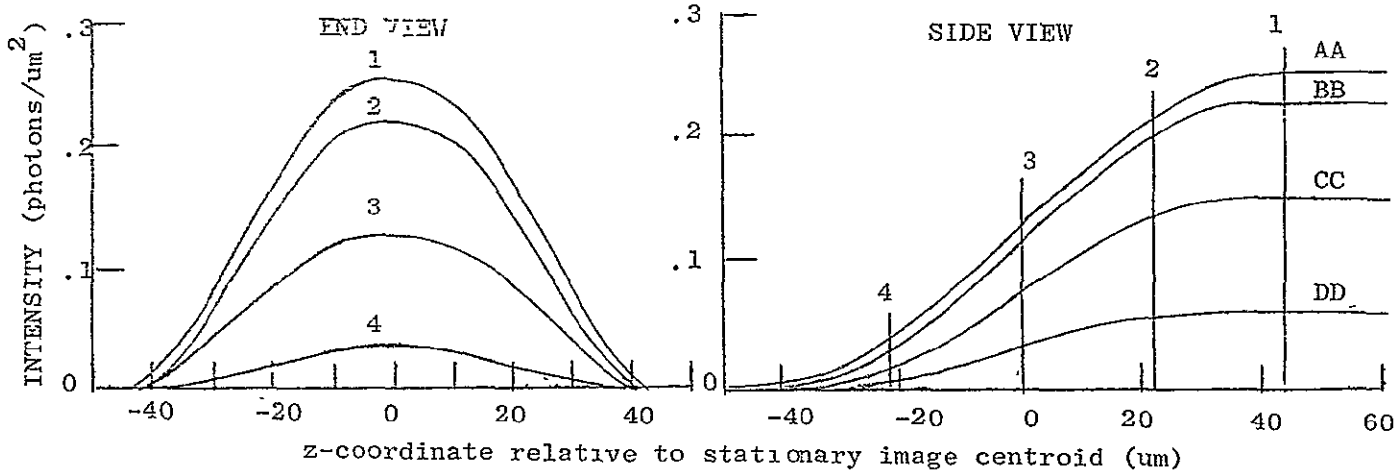

Fig. A-4 Scanned Image Shape During 5 arcminute Square Wave Chop to Right

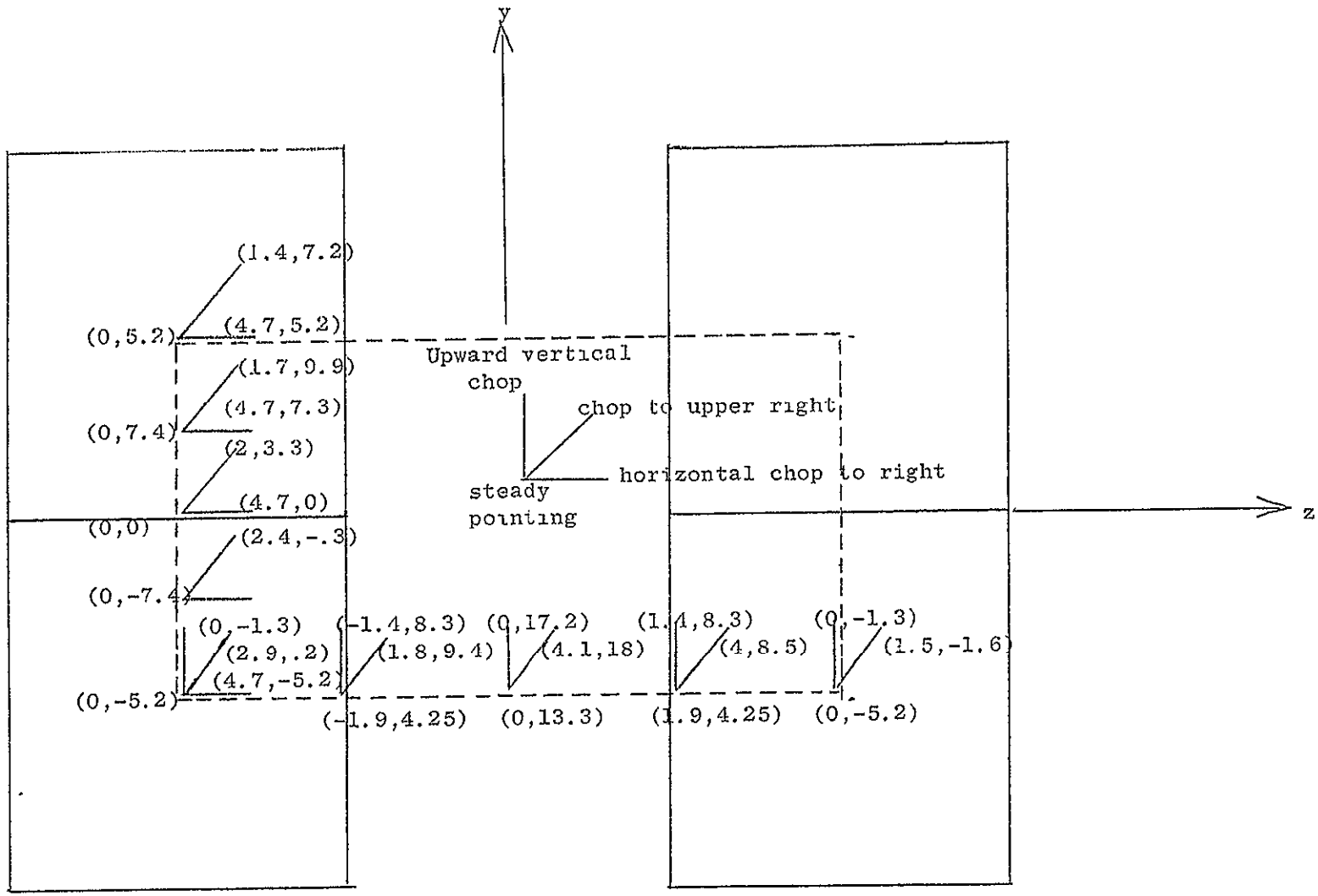

(dz,dy) interpolation errors in horizontal and vertical directions respectively (in units of 10^{-3} pixels)

Fig. A-5 Interpolation Errors with and without Chopping